

San Jose State University
SJSU ScholarWorks

Master's Theses

Master's Theses and Graduate Research

Fall 2009

Effects of wall compliance on pulsatile flow attenuation in microchannels.

Jing-Keat Goh
San Jose State University

Follow this and additional works at: https://scholarworks.sjsu.edu/etd_theses

Recommended Citation

Goh, Jing-Keat, "Effects of wall compliance on pulsatile flow attenuation in microchannels." (2009). *Master's Theses*. 3990.
DOI: <https://doi.org/10.31979/etd.wuhc-nxq9>
https://scholarworks.sjsu.edu/etd_theses/3990

This Thesis is brought to you for free and open access by the Master's Theses and Graduate Research at SJSU ScholarWorks. It has been accepted for inclusion in Master's Theses by an authorized administrator of SJSU ScholarWorks. For more information, please contact scholarworks@sjsu.edu.

NOTE TO USERS

This reproduction is the best copy available.

UMI[®]

EFFECTS OF WALL COMPLIANCE ON PULSATILE FLOW ATTENUATION IN
MICROCHANNELS

A Thesis

Presented to

The Faculty of the Department of Mechanical and Aerospace Engineering

San José State University

In Partial Fulfillment

of the Requirements for the Degree

Master of Science

by

Jing-Keat Goh

December 2009

UMI Number: 1484323

All rights reserved

INFORMATION TO ALL USERS

The quality of this reproduction is dependent upon the quality of the copy submitted.

In the unlikely event that the author did not send a complete manuscript and there are missing pages, these will be noted. Also, if material had to be removed, a note will indicate the deletion.



UMI 1484323

Copyright 2010 by ProQuest LLC.

All rights reserved. This edition of the work is protected against unauthorized copying under Title 17, United States Code.



ProQuest LLC
789 East Eisenhower Parkway
P.O. Box 1346
Ann Arbor, MI 48106-1346

© 2009

Jing-Keat Goh

ALL RIGHTS RESERVED


SAN JOSÉ STATE UNIVERSITY

The Undersigned Thesis Committee Approves the Thesis Titled
EFFECTS OF WALL COMPLIANCE ON PULSATILE FLOW ATTENUATION IN
MICROCHANNELS

by

Jing-Keat Goh

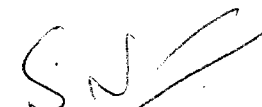
APPROVED FOR THE DEPARTMENT OF
MECHANICAL AND AEROSPACE ENGINEERING



Dr. John Lee, Department of Mechanical Engineering Date 11/6/09




Dr. Jinny Bhee, Department of Mechanical Engineering Date 11/3/09



Dr. Narayan Sundararajan, Intel Corporation Date 11/9/09

APPROVED FOR THE UNIVERSITY



Associate Dean Office of Graduate Studies and Research Date 12/3/09

ABSTRACT

EFFECTS OF WALL COMPLIANCE ON PULSATILE FLOW ATTENUATION IN MICROCHANNELS

by Jing-Keat Goh

The attenuation of pulsatile flow through highly compliant microchannels has been investigated. The expansion of a compliant microchannel subjected to pulsatile flow is able to store fluid temporarily and thereby reduce the peak-to-peak magnitude of flow fluctuation. In a highly compliant microchannel, the microchannel expansion reduces its hydraulic resistance and its associated pressure drop. For a similar inlet pressure condition, the pressure drop along the length of a more compliant microchannel is lower than a rigid microchannel. Therefore, greater net pressure is available to deform the microchannel wall. So the hypothesis of this study is the coupled relationship between higher pressure and greater wall compliance which will achieve more effective flow stabilization, because both contribute synergistically to greater volumetric expansion. To investigate this hypothesis, a soft elastomer, polydimethylsiloxane was used to compare plain microchannels and microchannels with a series of laterally deformable membranes, which vary in terms of wall compliance. In a 6 Hz pulsatile flow experiment, a membrane microchannel is able to achieve a better pulsatile flow attenuation ratio of 16 when compared to a plain microchannel pulsatile flow attenuation ratio of 10. The hypothesis was also investigated with a 2-D fluid-structure interaction numerical model and the prediction is in agreement with experimental results. The results indicate that higher compliance microchannels have better pulsatile flow attenuation abilities.

ACKNOWLEDGEMENTS

First, I would like to thank my committee chair and advisor, Professor John Lee, for support, ideas, and the opportunity to work at the Microelectromechanical Systems (MEMS) Laboratory. His teaching and guidance have been invaluable and have enabled me to grow as a researcher and engineer. I would also like to thank Dr. Jinny Rhee, Dr. Narayan Sundararajan and Dr Ji Wang for their interest and insightful feedback. I would like to thank all MEMS Laboratory friends, who provided assistance during the thesis. Paul Morris has been a great lab colleague, and I thank him for providing fabrication, testing assistance, as well as engaging in interesting discussions.

Microfluidic chip fabrication was made possible through Microscale Process Engineering Laboratory. Finally, I would like to extend my deepest thank to my parents for their continuous encouragement and to Yee-Tang Tan, for patiently supporting my endeavors.

TABLE OF CONTENTS

List of Tables	ix
List of Figures	x
Chapter 1 Introduction	1
1.1 Background	1
1.2 Motivation for Flow Stabilization	6
1.3 Proposed Pulsatile Flow Stabilization Device	7
1.4 Hypothesis	9
Chapter 2 Related Work	10
2.1 Compliant Conduits	10
2.2 Flow Stabilization	11
2.3 Dynamic Flow Characterization	14
2.3.1 Fluid-Structure Interaction (FSI) Simulation	14
2.3.2 Lumped Parameter	16
2.3.3 Experimental Methods	16
Chapter 3 Theory and Modeling	20
3.1 Fluidic Dynamics Theory	20
3.1.1 Navier-Stokes Equation	20
3.1.2 Steady Flow	21
3.1.3 Pulsatile Flow in a Rigid Conduit	23
3.1.4 Pulsatile Flow in Compliant Conduit	25

3.1.5 Hydraulic Circuit Theory	26
3.2 Mechanics of Hyperelastic Materials.....	31
3.3 Numerical Simulation	35
3.3.1 Arbitrary Lagrangian-Eulerian (ALE)	35
3.3.2 Entrance Length	38
3.3.3 Simulation Model Definition and Boundary Condition.....	39
Chapter 4 Experimental Methods	44
4.1 Microfluidic Chip Fabrication	44
4.2 Experimental Plan and Procedures	49
4.3 Uncertainty Analysis.....	52
Chapter 5 Results and Discussion.....	54
5.1 Experiment Results and Discussion.....	54
5.1.1 Step Pressure Results	54
5.1.2 Pulsatile-Wave Results	57
5.2 Simulation Prediction.....	63
5.2.1 Step Pressure Prediction	63
5.2.2 Pulsatile Pressure Prediction.....	65
5.2.3 Simulation of the Cross-Section Deformation of Compliant Microchannels..	70
Chapter 6 Conclusion and Future Work	74

Bibliography	79
Appendix I Optimization of SU-8 Fabrication	92
Appendix II SU-8 Fabrication Log	95

LIST OF TABLES

Table 1 Summary of fluidic circuit and electrical circuit equivalence	30
Table 2 Summary of hyperelastic models categorized according derivation origins	31
Table 3 Entrance length of different flowrate.....	39
Table 4 A summary of simulation boundary condition.	42
Table 5 Time dependent pressure condition at the inlet of the microchannel.	43
Table 6 Bill of material of the fluidic control and measurement system.....	51
Table 7 Uncertainty specification of pressure sensors in percentage full span	53
Table 8 Summary of pressure sensor uncertainty	53
Table 9 Extracted rise time and cutoff frequency from Figure 18.....	56
Table 10 Measured resistance and estimated capacitance of a 40 mm microchannel	56
Table 11 Comparison of RMS average outlet pressure at 2 Hz, 4 Hz, 6 Hz	58
Table 12 Comparison of expanded area of membrane channel and plain channel.....	72
Table 13 Comparison of capacitance estimated from experimental method, and numerical method.....	73
Table 14 Viscosity comparison between SU-8 2035 and 2050 [97]	93
Table 15 Comparison of original and optimized baking time	94

LIST OF FIGURES

Figure 1 Left, top view of laterally deformable membrane in a microchannel. Right, cross-sectional view of the membrane microchannel.....	8
Figure 2 Experimental setup for measuring hydraulic resistance dynamics.....	17
Figure 3 Schematic of a micro PIV setup on an inverted microscope.....	18
Figure 4 A 2-D pulsatile flow in a rigid conduit.....	24
Figure 5 Left, fluid flow through a tube with a balloon. Right, flow in a thin membrane microchannel, analogous to the tube/balloon system.....	25
Figure 6 Pulsatile flow in a compliant conduit. F	26
Figure 7 2-D approximation of the membrane deformation, cross-section view	27
Figure 8 Equivalent circuit modeling of a single unit membrane.....	30
Figure 9 Fitted Mooney-Rivlin planar stress-strain curve to measured stress.....	34
Figure 10 Fitted Mooney-Rivlin uniaxial stress strain curve to measured stress	34
Figure 11 COMSOL Multiphysic geometry of simulated plain microchannel (top) and simulated membrane microchannel (bottom) for comparative simulation.....	40
Figure 12 Layout of photo mask.....	44
Figure 13 Fabricated SU-8 based mold structure on silicon wafer.....	46
Figure 14 Cross section of a SU-8 membrane microchannel mold.	46
Figure 15 A microfluidic test chip attached with polymer tubing compared to a US penny.	48
Figure 16 Diagram of the fluidic control and measurement system.....	50
Figure 17 Actual fluidic control and measurement hardware.....	51

Figure 18 Step rise of a plain and 2 mm membrane microchannel (40 mm).....	55
Figure 19 Outlet pressure wave of a plain vs. 2mm membrane long (40mm) microchannel at 2 Hz.....	59
Figure 20 Outlet pressure wave of a plain vs. 2mm membrane long (40mm) microchannel at 4 Hz.....	59
Figure 21 Outlet pressure wave of a plain vs. 2mm membrane long (40mm) microchannel at 6 Hz.....	59
Figure 22 Normalized 2 Hz inlet and outlet pressure wave.....	60
Figure 23 Normalized 4 Hz inlet and outlet pressure wave.....	61
Figure 24 Normalized 6 Hz inlet and outlet pressure wave.....	61
Figure 25 Attenuation ratio of the normalized RMS average of inlet and outlet pressure.....	62
Figure 26 Inlet pressure of a simulated plain and simulated membrane microchannel due to a step pressure input.	64
Figure 27 Plot of the normalized inlet flowrate and inlet pressure of a simulated membrane microchannel	64
Figure 28 Predicted flowrate of compliant microchannels at 2 Hz pressure wave.....	66
Figure 29 Predicted flowrate of compliant microchannels at 4 Hz pressure wave.....	66
Figure 30 Predicted flowrate of compliant microchannels at 6 Hz pressure wave.....	66
Figure 31 Flow attenuation ratio of thick membrane (left) and thin membrane (right) ...	67
Figure 32 Top, the predicted thick membrane deformation is 2 μm . Bottom, the predicted thin membrane deformation is 9.8 μm	68

Figure 33 Pressure drop of thin microchannel vs. thick microchannel along the length of microchannel	68
Figure 34 Simulation plots of cross-section of membrane microchannel and plain microchannel under 20 kPa load with a step size of 5000Pa	72
Figure 35 Picture shows section of SU-8 structure with poor photolithography resolution	92

Chapter 1 Introduction

1.1 Background

The concept of using microfluidics to miniaturize control and manipulation of fluids has increasingly been used to develop devices that are capable of automating laboratory tasks [1, 2]. Microfluidic devices are not simply networks of conduits. Rather, they can include miniaturized laboratory components such as pumps, valves, mixers, optics, and sensors [3]. Highly integrated microfluidic devices are also capable of accomplishing many complex chemical or biological reactions with little or no manual intervention, hence reducing human errors. The integrated chips are sometimes referred to as “lab on a chip” (LoC) devices, micro total analysis systems (μ TAS) or miniaturized analysis systems [4]. The small length scale of a microfluidic device has many system design and fabrication advantages when compared to its macroscale counterpart. A microfluidic device uses a small amount of reagents and generates minimal waste, hence resulting in overall cost saving. Microfluidic systems are highly scalable so that similar analyses can be performed in parallel on a single device, increasing throughput [5]. The micro-length scale also improves speed, sensitivity, accuracy, and repeatability of many reactions [6].

The recent advancement of human genome sequencing, biotechnology, and growing health care problems has accelerated the development of microfluidic systems to automate laboratory experiments that may otherwise be slow, expensive, or labor-intensive. In a typical heart attack situation, for example, the patient would require a

prompt diagnostic such as electrocardiogram and blood test. While blood testing is typically done in a laboratory environment, a microfluidic portable system can provide a rapid diagnosis of the patient's cardiac condition [7]. After the user dispenses a few drops of blood into the sample port, the blood is filtered and mixed with reagents. The system can rapidly provide the test results in approximately 15 min. This system is an example of a microfluidics-enabled point-of-care system where a health care provider can monitor the condition of a patient faster and on site. Manipulating biological fluids with microfluidic devices is appropriate because biological cells and blood vessels are in the micron scale. Flow cytometry systems that sort and count particles or cells, often involve large instruments. Besides consuming a large volume of reagents, the system also requires a trained specialist to competently perform pre-treatment steps and to operate the hardware. Microfluidic based flow cytometry, together with solid-state optics, can accomplish a similar analysis with only nanoliters of reagents. This also allows the monitoring cells at the molecular level with high accuracy [8].

Drug discovery benefits from the automation provided by a microfluidic device in sample handling, reagent mixing, separation, and detection [9]. Recently, researchers have developed a microfluidic chip that is capable of performing 1000 simultaneous chemistry reactions [5]. These reactions are able to screen potential drug candidates by identifying chemicals that bind to proteins through mass spectrometry. The device accomplishes the reactions rapidly with high throughput. Parallel to advancement in drug discovery, microfluidics based drug delivery methods are also being developed. An array of microneedles that is capable of penetrating the skin layer has been developed to deliver

drugs in a less painful fashion by avoiding nerve receptors [10]. This delivery system can furthermore be integrated with closed loop feedback control of drug levels in the body, thus dispensing optimum drug dosages [11, 12].

Developing such microfluidic devices requires the understanding of fluid behavior at a micro scale, which is different than in the macro world. This is because the fluidic behavior changes dramatically as size decreases [13]. An example is laminar flow in microchannels, for which viscous effects dominate mass transport, whereas in a macro scale conduit inertial effects are dominant. Understanding and developing models to quantify these unique fluidic phenomena are crucial for effective design of microfluidic systems. One of the well-known applications of laminar characteristics is particle filtration through laminar diffusion [14]. By introducing adjacent particle-laden and particle-free streams, particles diffuse into the particle free stream. While the diffusivity of the particles is a function of particle size, the size of particle filtration is achieved by controlling the flowrate and channel length, such that larger particles do not have enough time to diffuse across the stream.

Another benefit of microchannel flow is the increased surface area to volume ratio, which provides a rapid heat transfer rate and precise temperature control. Capitalizing on this heating behavior, a microreactor based on microfluidic technology can enable chemical reactions to be performed with very precise control [6]. Fluid temperature can be rapidly increased or decreased by moving fluids through micro-heat exchangers. The rapid and precise temperature cycling enables the reactors to control secondary reactions and the creation of undesired byproducts after the primary reaction is

complete. Subsequently, the process can yield higher purity of the desired products when compared to its macro counterpart. The rapid heating ability of a microchannel is also commonly utilized in commercial inkjet printers. Printer nozzles are made from arrays of microchannels with heating elements. They dispense droplets of ink when an electrical current is applied to the heating element [15]. In addition, the enhanced heat transfer property has also generated interest in using microfluidics for cooling high heat flux power electronics. Jiang et al. reported a heat removal system with micro-machined channels on a silicon substrate coupled with an electro-osmotic pump and a heat exchanger [16, 17]. The group claimed that the system is capable of removing 38 W from a 1 cm by 1 cm silicon chip. The list of novel microfluidic applications extends further beyond the scope of this brief introduction with usage such as microfluidic fuel cells, microfluidic chips for environment analysis and micro-propulsion [18-20].

Early microfluidic chips were manufactured from silicon or glass with semiconductor etching methods. These techniques have required expensive equipment and a variety of toxic and corrosive chemicals. Hence, a significant amount of work has been dedicated to discover alternative materials, especially polymers [21, 22]. Polymers are usually more economical and can be fabricated using convenient molding or embossing method. However, polymers are incompatible with many organic solvents and high temperatures [23]. In this study, the microfluidic test samples are made of polydimethylsiloxane (PDMS) elastomer. PDMS is very attractive for research based rapid prototyping and fabrication can be done in simple laboratory settings [23]. PDMS has many desirable properties for microfluidic applications such as bio-compatibility and

good optical transmittance down to 280 nm, which are important for both bio-samples detection and imaging [1, 23, 24]. In addition, PDMS is gas permeable, and this can be advantageous for filling dead end channels or allowing oxygen flow to support cell cultures [13]. The material is hyperelastic and even has a tunable modulus of elasticity that is strongly dependent on the ratio of curing agent to pre-polymer [25]. PDMS has been adapted to develop many versatile microfluidic components such as microvalves and micropumps [26, 27]. The low cost of microfluidic chips made from polymers such as PDMS makes it economically viable to make disposable chips, thereby eliminating cross contamination of analyses and reactions [2, 28].

1.2 Motivation for Flow Stabilization

An integrated microfluidic chip usually consists of a pumping mechanism to drive flow through a microchannel. In a comprehensive review of micropumps by Laser and Santiago, micropumps can be grouped into two categories; these are the displacement and dynamics types [29]. Under displacement type micropumps, the authors further distinguished the motion of the micropumps by reciprocating type, rotary type and aperiodic type. The review reported that reciprocating displacement type micropumps are in fact the most widely researched micropumps. The majority of the displacement type micropumps rely on some periodic forces acting on a diaphragm to push fluids through conduits, thus inevitably producing unsteady or pulsatile type flows. However, displacement type micropumps are easier to implement in microfluidic devices because the pumps are not dependent on the type of fluids. For instance, the pumping rate of a displacement micropump is not affected by viscosity because the pumping rate is determined by squeezed volume [30]. Unlike dynamic type micropumps such as electrohydrodynamics, electro-osmotic or magnetohydrodynamics micropumps, which produce smoother flow, the displacement type micropumps do not require ionic fluids or special surface pre-treatments [29, 31]. Most microfluidic labs are equipped with syringe pumps as flow driving sources due to its off-the-shelf availability and flowrate controllability. A syringe pump is driven by a stepper motor rotating a lead screw, which in turn moves a metal block compressing a syringe plunger. The stepper motor usually rotates at a very small, but abrupt angles cause the generated flow to be pulsatile in nature [32, 33].

Regardless of the pumping mechanism, pulsatile flow might be desirable or undesirable, depending on application. Pulsatile flow is usually used to introduce fluid turbulence which is important in applications such as reagent mixing [34]. Conversely, smooth flow is desirable in applications such as flow cytometry. Fluid flow transients, resulting from pumping mechanisms, are known to affect important flow cytometry performance characteristics, such as stream alignment, particle speed, stability of flow, and particle detection rate [35]. To overcome this problem, Honeywell has made significant efforts to investigate non-pulsatile micropumps for microfluidic flow cytometry [36]. Flowrate accuracy, precision and pulsatility can also negatively impact the sensitivity of high performance liquid chromatography (HPLC) [37]. Pulsatile flow also causes a higher variation of apparent refractive index of mobile phase, which reflects as a higher baseline noise when the flow passes through sensors [37]. Basic flowrate accuracy and precision can be directly improved with a smooth flow which would allow for more precise flow metering.

1.3 Proposed Pulsatile Flow Stabilization Device

This thesis studies pulsatile flow stabilization with compliant microchannel walls, in particular comparing a regular rectangular cross-section microchannel and a laterally deformable thin-wall microchannel. The regular rectangular microchannel will be referred to as a plain microchannel. Laterally-deformable microchannel walls, also referred to as membranes are versatile and have been demonstrated in the past to perform various microfluidic operations [26, 38]. Different membrane arrangements and actuation profiles can be used to construct microfluidic components such as valves,

micropumps, particle sorters and mixers. The membrane can be easily integrated into a microfluidic chip because of its ease of fabrication, explained further in Section 4.1.

Deformable membranes, when integrated along a microchannel, can enhance structural compliance and improve flow stabilization. The operation principle of deformable-microchannel walls is illustrated in Figure 1. The deformation of the membranes is caused by the fluidic pressure in the microchannel acting on the deformable membranes. The low pressure side of the membranes is assumed to be atmospheric pressure and can be pressurized if desired.

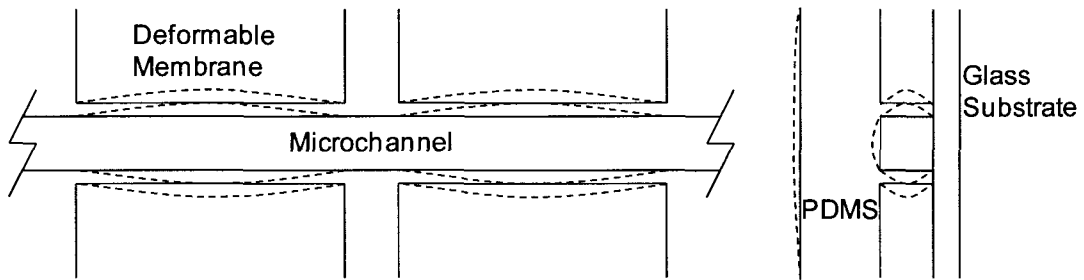


Figure 1 Left, top view of laterally deformable membrane in a microchannel. Dash lines indicate deformed shape. Right, cross-sectional view of the membrane microchannel.

1.4 Hypothesis

Highly compliant microchannel walls affect both capacitance and resistance in a coupled manner, which results in greater attenuation. During a pressure driven flow, the walls of a microchannel lined with compliant membranes deform by a larger magnitude than those of a plain microchannel, therefore increasing the overall microchannel cross-section and reducing overall resistance. The reduction in resistance further increases the average pressure along the length of the microchannel, and the larger pressure applies a larger force to the compliant wall to a larger degree. As a result, the larger expansion-contraction motion is more capable of stabilizing a pulsatile flow. More conventional circuit modeling theory assumes a fixed resistance and does not account for the lower resistance due to the expanded cross-section of the microchannel. To investigate this interdependency, a coupled fluid-structure interaction numerical simulation is performed to observe the relationship between compliance and pressure distribution. The actual inlet and outlet pressures of pulsatile flow through a plain microchannel and a membrane microchannel are measured experimentally. The compliant membrane microchannel is expected to have less pressure loss and subsequently better flow attenuation.

Chapter 2 Related Work

2.1 Compliant Conduits

Any non-rigid material, particularly a soft elastomer such as PDMS, is subjected to distortion in response to fluid pressure. The deformed channel can drastically alter flow characteristics because hydraulic resistance has a fourth power dependence on channel length scale, with respect to a channel cross-section [39-43]. In contrast, a traditional rigid conduit maintains its cross sectional shape during a pressure driven flow.

Fluid flow through a compliant conduit has generated significant research interest. Oates studied fluid flow through soft tubes in 1975, well before widespread interest in microfluidics [44]. Reuben studied pulmonary arterial compliance and identified that when arterial walls are stiff, a patient can suffer severe pulmonary hypertension [45]. In microfluidics, Wu et al. studied the way in which pressure-driven flow deforms microchannels and developed a set of theories to match such experimental results [43]. Gervais et al. studied the deformation of shallow microchannels with confocal microscopy, and they concluded that a low height-to-width aspect ratio microchannel would experience significant cross-section deformation [39]. Deformation along the length of the channel was found to be non-linear, resulting in fluid acceleration and difficulties with respect to precise metering. Hardy et al. extended the work of Gervais et al. by characterizing deformation of flexible PDMS microchannels under pressure-driven flow by using fluorescence microscopy [40]. By injecting rhodamine dye with mercury-vapor lamp illumination, the group recorded fluorescent images and measured fluidic pressure at multiple locations. They compared structural deformation by assuming a

linear dye-layer thickness and intensity relationship which was proportional to channel-wall deformation. They found that a pressure drop in a compliant ceiling microchannel can be up to 35% less than a rigid-ceiling microchannel due to larger flow cross-section. While both studies of Hardy and Gervais provide a steady state understanding, these particular investigations were not focused on the dynamic fluid behavior inside a compliant microchannel.

2.2 Flow Stabilization

In principle, flow stabilization can be achieved with any combination of mechanical or fluidic elements that exhibit fluidic storage and viscous dissipation behavior. Fluidic storage, also known as fluidic capacitance, is the ability to temporarily store fluid. Capacitance can be manifested using principles of gravity, fluid compression, wall elasticity, and capillary forces [46]. In a typical wall elasticity case, the fluidic pressure deforms an elastic wall and creates a temporary increase in fluidic volume. Viscous dissipation, known as hydraulic resistance, is the energy required to overcome fluidic shear stress. A fluidic resistor can be manifested as some form of flow constrictor such as a ceramic filter or a narrow microchannel cross-section [47, 48].

Yang et al. proposed a flow stabilizer device with a thin PDMS membrane sandwiched between a drilled glass slide and a PDMS chip [49, 50]. Their device was capable of attenuating pulsatile flow produced from a set of syringe pumps programmed with sinusoidal flowrate. However, the investigation was conducted using relatively large channels, with a cross-section of 5000 μm wide, 110 μm high. In another paper, the same group also proposed a microfluidic diode that was capable of regulating flow in a

single direction and stabilizing pulsatile flow [51, 52]. The diode was constructed with a thin PDMS slab, which was able to deform and alter flow cross-section, therefore regulating flowrate. Inman et al. implemented a flow stabilization concept using a compliant membrane in their design of a constant flow pneumatic micropump [48]. Their integrated micropump was built from a set of fluidic valves and a pumping chamber actuated by compressed air. The mechanical features were constructed from sandwiching a thin sheet of soft polymer onto a set of machined cavities. A separate open membrane chamber together with a fluid filter was located downstream in order to stabilize the periodic nature of the flow. In principle, the micropump, flow stabilizer, and the microfluidic device can be integrated in a simple single layer photolithography step, reducing manufacturing complexity. Debiotech, a commercial medical device company also developed a passive micro-flow regulator for drug delivery systems [53]. Their concept was to increase hydraulic resistance when fluid pressure suddenly increases, thereby reducing peak flow and generating a constant outlet flowrate. The device involved stacking three layers of micromachined silicon and glass. A deformable silicone structure that was capable of sealing against a long circular micromachined groove was used to temporarily create additional conduit length during sudden fluidic pressure rise.

Multiple research groups also investigated alternative pumping methods to produce a steady flow. Atencia and Beebe investigated a disk pump used to generate a steady flow for particle separation [54]. The disk pump consisted of a ferromagnetic bar in a circular chamber, and it was externally driven by a laboratory magnetic stirrer. They

demonstrated that the system was able to separate particles based on size without disturbing the concentration of larger particles with steady flow. Pulsatile flow can cause cross flow in a particle separation application and thereby reduce separation effectiveness. Namasivayam et al. investigated a continuous and low-flow velocity micropump based on transpiration [55]. Their design used an evaporation chamber with a liquid meniscus maintained by selective hydrophobic patterning. With controlled active air circulating in the chamber, fluid was evaporated, creating a constant fluid flow from the reservoir. They stated that smooth and low-flow velocity micropumps can be used to study single molecule assays such as DNA stretching, subcellular processes of mitochondrial movement and changes in cytoskeletal structure [56, 57].

Although these micropumps were able to produce smooth flow, they had very a low pressure head and involved more complex fabrication steps. Given the complexity of generating a smooth flow, it is invaluable to have a universal pulsatile flow rectifying device that is passive and easily integrated into the current microfluidic chip design. A passive microflow stabilizer offers the following advantages: simple design, no power consumption, no control circuitry and compatibility with other fluidic components. In addition to the above mentioned benefits, the PDMS deformable membrane studied in this thesis is very robust and insensitive to most physicochemical reactions.

2.3 Dynamic Flow Characterization

The study of flow stabilization requires a time-dependent methodology in order to capture the fluidic dynamics. Some distinct approaches include numerical simulation, lumped parameter modeling, and experimental methods. These methods are reviewed below in the context of dynamic flow characterization and modeling.

2.3.1 Fluid-Structure Interaction (FSI) Simulation

Fluid-structure interaction (FSI) is the study of the interaction of a deformable structure with its surrounding fluid. FSI becomes an important consideration when moving walls are physically manipulating fluid or fluid pressure is deforming the compliant structure. Blood flow through arteries is an example of fluid-structure interaction. FSI modeling is spatially and temporarily complex, and is therefore best suited for numerical simulation.

Several related FSI numerical studies on microfluidic devices have been published. Bozhi et al. simulated a microfluidic diode that considered fully coupled fluid structure interaction [58]. They were able to predict PDMS deformation, flowrate, and pressure distribution of the device with good experimental agreement. Klein et al. attempted to model a silicon and glass based micropump for aiding design optimization [59]. Their modeling involved multiple physics domains. The work included an electromechanical analysis, where the micropump membrane was actuated by a piezo-crystal, a fluid-structure interaction analysis, where the membrane pushed against fluid, and a thermo-fluid dynamic analysis, where heat was used to control fluid viscosity. The coupling of multiple physics domains caused a rather large model, so they built

individual physical coupling models with finite element methods and integrated them as lumped network elements. In another related study, Jeong et al. developed a so-called “self-generating” peristaltic micropump that can be controlled with a single source of compressed air [60]. The micropump consisted of 3 membranes in a series and a long narrow intermediate cross-section connecting the membranes, hence resulting in individualized membrane time constants. When a pressure waveform was introduced, the deformation was sequential like a peristaltic pump. The authors modeled the micropump pneumatic actuation with finite element software in order to predict membrane displacement and pressure distribution when actuated with a pressure source. They further characterized the capacitance of the membrane and found a non-linear capacitance relationship, caused by membrane contact with the microchannel wall.

2.3.2 Lumped Parameter

While a finite element model provides the finer details on flow and structural characteristics, it often involves higher computational cost and is limited to smaller simulation spaces. In contrast, lumped parameters can be used to analyze a large fluidic network with little computational complexity and resources [61]. The lumped parameter model approximates distributed properties such as resistance and capacitance of a conduit as discrete elements. The technique resembles the circuit modeling of electronic circuits, for which individual hardware components are replaced by abstracts elements.

Displacement type micropumps for microfluidic devices are one of the most popular devices modeled with lumped parameters [60, 62, 63]. This is due to the good analogy of a compliant membrane storing and discharging fluid as a capacitor, while viscous dissipation in a conduit resembles a fluidic resistor. Lumped parameter modeling can also be used to represent other physical interactions such as electrokinetic driven flow and heat transfer [64-66].

2.3.3 Experimental Methods

Regardless of what simulation method is used (i.e., numerical versus lumped-parameter), experimental methods are necessary to validate any model predictions. Kim et al. presented an experimental method for dynamic system characterization using the concept of hydraulic series resistance [47]. As shown in Figure 2, the system consists of two simple pressure sensors, a glass tube, and a microfluidic test chip. The pressure sensors were connected to a high speed data acquisition system to measure pressure P1 and P2, while the outlet of the microfluidic chip was assumed to be atmospheric. Since

the glass tube was a known fixed fluidic resistor, flowrate can be estimated by dividing pressure difference and resistance. The system was able to measure flowrate with a high sampling rate, which is unachievable with flow sensors based on thermal sensing principles. The group also investigated flow through a compliant microfluidic chip and found pressure to decrease with increasing compliance in the microchannel. Furthermore, a step change in pressure was introduced into the compliant microchannel and the corresponding rise time for a compliant microchannel was found to be significantly longer than for a rigid channel, consistent with theory.

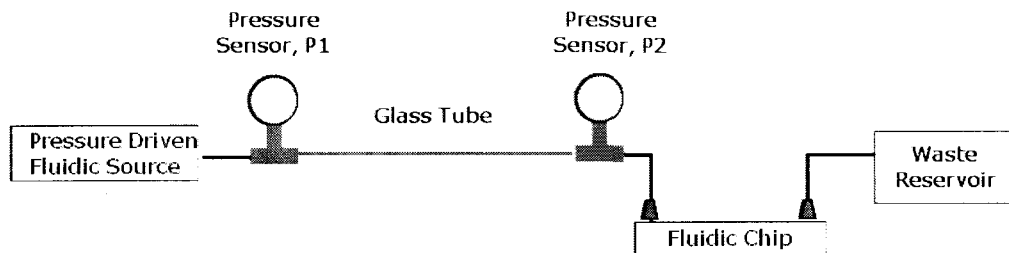


Figure 2 Experimental setup for measuring hydraulic resistance dynamics (based on [47])

Dynamic fluidic behavior can also be monitored with particle visualization methods such as particle image velocimetry (PIV). Typically, the fluid is seeded with particles or markers and it is assumed that the particles will follow the streamlines of the flow. PIV techniques have been used in macro scale fluid flow visualization such as fluid flow in a pipe or wind tunnel [67]. Micro particle image velocimetry (μ PIV) is an extension of PIV used to accommodate microfluidics devices. A μ PIV setup consists of a microscope (upright or inverted), camera (CCD or CMOS), particle illumination source (laser), appropriate optics (oil-immersion objective lens, filters and beam expander) and fluorescent dyed tracer particles. μ PIV has the merit of being a noninvasive, full-field

measurement tool since cells or particles can be stained and directly imaged. Figure 3 describes the arrangement of a typical μ PIV system.

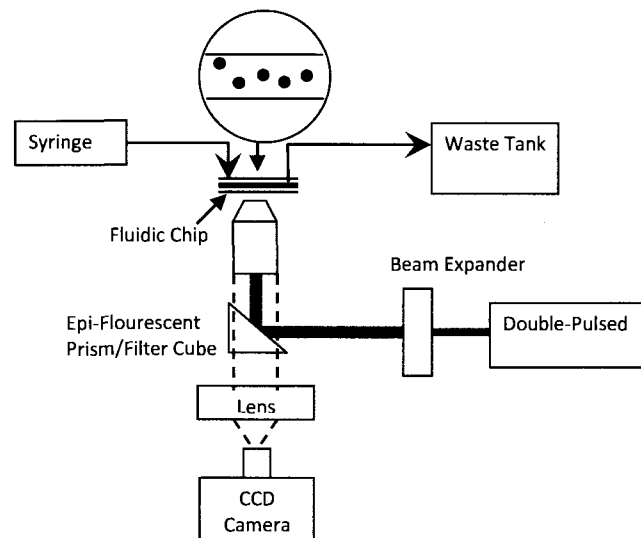


Figure 3 Schematic of a micro PIV setup on an inverted microscope (based on [22])

The fluid flow visualization is typically done by illumination of fluorescent particles by a double pulsed, frequency doubled Nd:YAG 532 nm wavelength laser. The laser excites the fluorochrome to a higher energy state, thus emitting photons with longer wavelength. To capture the long wavelength light, a long pass filter is used to reduce the reflected laser light thus reducing noise. In a good fluorescent selection practice, one will select a significantly longer wavelength emission fluorescent bead to effectively filter out the illumination source. Selection of particle size and concentration is another important consideration in a μ PIV device. First, the particles need to have enough surface area (size) to emit sufficient light in order to be properly captured and to avoid Brownian motion [68]. Second, the particle sizes have to be small enough so that they will not alter the flow and cause channel blockage. Third, particle concentration has to be on the optimum level to reduce signal to noise ratio [69]. μ PIV is an emerging tool to

investigate microfluidic device and microflow. Santiago et al. first developed a μ PIV measurement system for microchannel flows [15, 17]. Wang et al. proposed using μ PIV for fluid flowrate measurement [14]. Their velocity profile measurement closely matched theoretical profile and can be used to calculate flowrate. Li et al. studied turbulent flows in microchannel under μ PIV and determined that the turbulent transition started around Reynolds number of 1700. Using μ PIV to measure pulsatile flow is possible given high enough image sampling rate as was demonstrated by Kim et al. [10]. While μ PIV offers full flow field visualization, the implementation is often costly due to high performance cameras and optics. After image acquisition is done, further image processing is required in order to extract velocity and flowrate.

Chapter 3 Theory and Modeling

3.1 Fluidic Dynamics Theory

3.1.1 Navier-Stokes Equation

In classical fluid mechanics, a fluid is assumed to be a continuum and is described by the Navier-Stokes equation. The equation is a nonlinear partial differential equation, as shown in Equation (1). It is derived from the principals of conservation of momentum and conservation of energy [70]. Here, \mathbf{u} is the velocity field, p is pressure, ρ is fluid density and μ is dynamic viscosity. For a microfluidic flow, the inertial forces are usually small compared to viscous forces, hence the equation can be reduce to the Stokes equation, shown in Equation (2). The Navier-Stokes equation is also complemented by the continuity equation because the inlet and outlet flows for a closed conduit are equal. For an incompressible fluid for which the fluid density does not change over time, the simplified continuity equation is shown in Equation (3).

$$\rho \left(\frac{\partial \mathbf{u}}{\partial t} + \mathbf{u} \cdot \nabla \mathbf{u} \right) = -\nabla p + \rho \mathbf{g} + \mu \cdot \nabla^2 \mathbf{u} \quad (1)$$

$$\rho \frac{\partial \mathbf{u}}{\partial t} = -\nabla p + \rho \mathbf{g} + \mu \cdot \nabla^2 \mathbf{u} \quad (2)$$

$$\nabla \cdot \mathbf{u} = 0 \quad (3)$$

3.1.2 Steady Flow

Microfluidic flow is well known for its laminar characteristic due to the length scale of the conduit cross-section [13]. The laminar characteristic can be verified by the Reynolds number (Re), which compares the ratio of inertial to viscous forces within fluid flow. The Reynolds number is a function of fluid density ρ , dynamic viscosity μ , diameter D and flow velocity v , as shown in Equation (4). For a square microchannel, the diameter of the conduit is estimated by the equivalent hydraulic diameter, D_h shown in Equation (5).

$$\text{Re} = \frac{\rho v D}{\mu} \quad (4)$$

$$D_h = \frac{2LW}{L+W} \quad (5)$$

As an example, the Reynolds number of a microchannel with hydraulic diameter of 40 μm , flow velocity of 100 mm/s with water as working fluid is found to be $\text{Re} = 4$. This suggests the fluid flow is dominated by viscous dissipation rather than fluid inertial effects. Applying the laminar flow characteristic with assumption of fully developed, incompressible and isothermal Newtonian fluid, the Navier-Stokes equation is solved and results in Hagen-Poiseuille flow. The Hagen-Poiseuille velocity profile for a channel with a rectangular cross-section is shown in Equation (6). Integrating the velocity profile in the normal direction results in volumetric flowrate, as shown in Equation (7) [65, 71]. After applying mathematical approximations and boundary conditions, the simple form of volumetric flowrate as a function of channel cross-section, length, fluid viscosity and pressure is obtained. The equations for a rectangular and a square microchannel are

shown in Equation (8) and Equation (9) respectively [65]. The developed model can be used to predict flowrate for a given pressure gradient of a fully developed laminar conduit. The resistance factor can also be independently extracted from the model in the form of Equation (10).

$$u_x(y, z) = -\frac{1}{2\mu L} P h^2 \left[1 - \left(\frac{z}{h}\right)^2 + 4 \sum_{n=1}^{\infty} \frac{(-1)^n}{(\alpha_n)^3} \frac{\cosh\left(\frac{\alpha_n y}{h}\right)}{\cosh\left(\frac{\alpha_n w}{h}\right)} \cos\left(\frac{\alpha_n z}{h}\right) \right] \quad (6)$$

$$\text{where } \alpha_n = (2n-1)\frac{\pi}{2}, n = 1, 2, 3, \dots$$

$$Q = \int u_x dA = \frac{4P}{3\mu L} wh^3 \left[1 - \frac{6h}{w} \sum_{n=1}^{\infty} \frac{\tanh\left((2n-1)\frac{\pi w}{2h}\right)}{\left((2n-1)\frac{\pi}{2}\right)^5} \right] \quad (7)$$

$$Q = P \frac{\left(1 - 0.63 \frac{h}{w}\right) h^3 w}{12\mu L} \quad (8)$$

$$Q = P \frac{h^4}{28.4\mu L} \quad (9)$$

$$Q = \frac{1}{R_{hyd}} \Delta p \quad (10)$$

3.1.3 Pulsatile Flow in a Rigid Conduit

Unlike uniform, steady flow, pulsatile flow involves acceleration of a fluid. Fluid acceleration can further be divided into acceleration in space and acceleration in time [72]. When fluid flows through a narrow region, its velocity increases to maintain flowrate and this mode of acceleration is referred as acceleration in space. The fluid acceleration in space is induced by the changing cross section, for which the local velocity profile does not change with time and the flow is steady. On the other hand, fluid acceleration in time means that the fluid velocity profile at a given position varies with time and is associated with unsteady flow. This mode of acceleration is caused by a time dependent driving pressure and is associated with pulsatile flow.

In steady-state fluid flow through a rigid conduit, a constant pressure gradient driving a flow is expected to produce a velocity profile characteristic of Poiseuille flow. A time dependent driving pressure gradient driving an oscillatory flow in a rigid conduit is also expected to produce a velocity profile characteristic of Poiseuille flow if the flow acceleration is in phase with the driving pressure. This type of system is termed quasi-static. In the event where the peak velocity of the pulsatile flow fails to reach the same velocity of a Poiseuille flow, the fluid inertial effect is dominant, therefore requiring examination of frequency dependence. The Womersley number α , which qualitatively evaluates the effects of pulsatile frequency on the viscous effects in the flow, is defined by Equation (11) [73]. The properties used to calculate α are pulsatile angular frequency ω , conduit radius r , fluid density ρ , and dynamic viscosity μ .

$$\alpha = r \sqrt{\frac{\omega \rho}{\mu}} \quad (11)$$

When α is less than unity ($\alpha < 1$), the pulsation of the flowrate is able to propagate through the channel and is considered to be in phase with respect to the oscillatory pressure gradient. Assuming a fully developed flow, the velocity profile is always parabolic throughout the conduit as shown in Figure 4. Therefore, the system behaves like a steady flow and can be approximated by the Hagen-Poiseuille equation. Conversely, when α is greater than unity $\alpha > 1$, the flow lags the applied oscillatory pressure and the velocity profile is plug-like. There is a departure from the fully developed steady flow assumption with increases in pulsatile frequency and conduit radius. Microfluidic conduits are in the micron scale, so the Womersley number is usually small. For example, a 50 Hz pulsatile water flow in a square microchannel with hydraulic diameter of 40 μm has a Womersley number of 0.354.

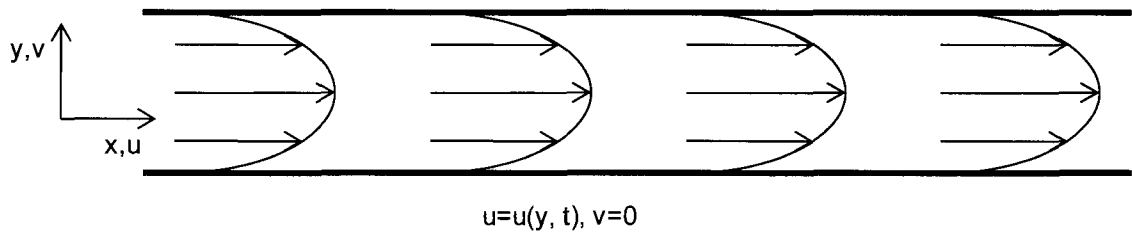


Figure 4 A 2-D pulsatile flow in a rigid conduit. The oscillating pressure changes the inlet and outlet velocity instantaneously when the Womersley number is small. Adapted from [74].

3.1.4 Pulsatile Flow in Compliant Conduit

Consider a conduit with a balloon connected at an intermediate location as shown in Figure 5 [72]. Fluid flow entering the conduit will expand and fill the balloon before exiting the conduit. The outlet flowrate is less than the inlet flowrate because of the volume of fluid is diverted to the balloon. The reduction in the outlet flowrate is analytically provided by application of conservation of mass, $Q_{out} = Q_{in} - Q_{store}$. Analogous to the balloon example in Figure 5, a PDMS compliant microchannel with membranes expands when the fluidic pressure gradient is applied on the microchannel wall. In a pulsatile flow case, elevated pressure will deform the channel and store fluid in the increased volume. Similarly, when the pulsatile pressure wave is at a reduced level, the elastic membrane collapses and fluid is returned to the conduit.

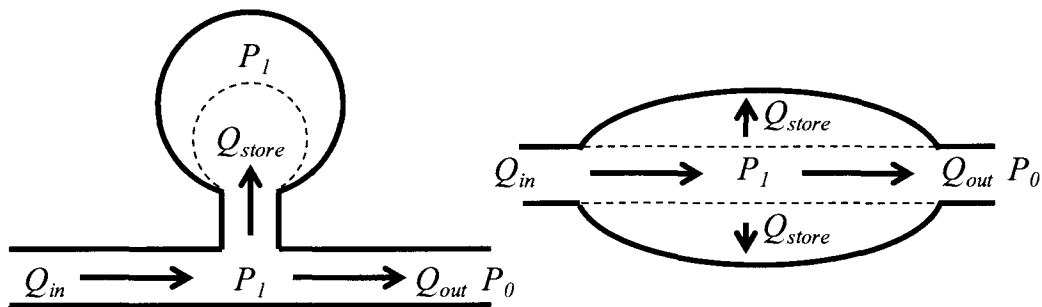


Figure 5 Left, fluid flow through a tube with a balloon. Right, flow in a thin membrane microchannel, analogous to the tube/balloon system. Adapted from [72].

Pulsatile flow in a compliant conduit is known to travel like a wave and can be reflected when meeting an obstacle [74, 75]. The reflected wave can also partially cancel the flow if the reflected wave is the opposite phase of the initial flow. The wave speed c_0 can be estimated by the Moen-Korteweg formula shown in Equation (12) and the wavelength can be estimated by Equation (13). In the equations, E is the modulus of

elasticity of the conduit wall, b is the wall thickness, ρ is the density of fluid, D is the diameter of the conduit and ω is the pulsatile angular frequency. In a rigid channel, the wave speed is almost infinite due to the very high modulus of elasticity. Therefore, travelling waves can be observed only in compliant conduits. The wave propagation constantly deforms the channel walls and causes fluidic acceleration in both space and time.

$$c_0 = \sqrt{\frac{Eb}{\rho D}} \quad (12)$$

$$L = \frac{2\pi c_0}{\omega} \quad (13)$$

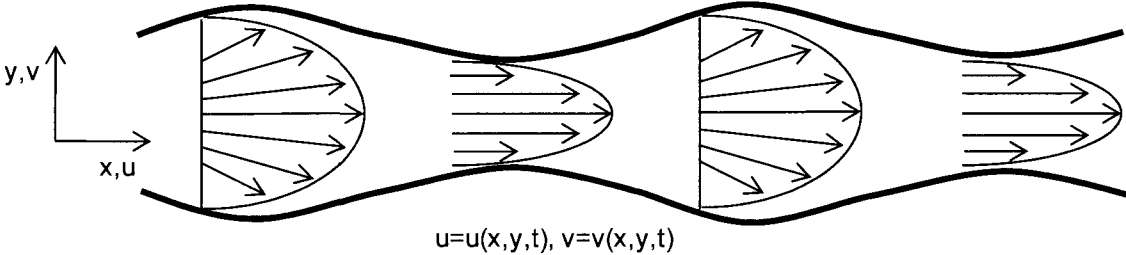


Figure 6 Pulsatile flow in a compliant conduit. Fluid deforms the elastic wall and the elastic wall rebound and move the fluid. Hence the fluid propagates downstream like a wave. Adapted from

[74].

3.1.5 Hydraulic Circuit Theory

Hydraulic circuit theory uses a lumped parameter approach to model fluidic components. As in Equation (10), the product of flowrate and hydraulic resistance gives pressure drop across the conduit. In contrast, Ohm's law states that electrical potential

drop or voltage, v is proportional to current, i , by electrical resistance, R_{el} [76]. Both fluidic viscous shearing and electrical resistance dissipate energy in the form of heat.

$$v = iR_{el} \quad (14)$$

Compliant microchannel walls expand and store fluid when a fluidic pressure is applied. The walls behave like a fluidic capacitor, defined by the change in pressure dP require to change the volume of the conduit dV , as expressed in Equation (15).

Analytically, the deformation of a compliant membrane can be modeled as uniform pressure acting against a thin plate. Since the microchannel is relatively long compared to its cross-sectional area, it may be assumed that the cross sectional deformation is similar along the channel length. Typically, the deformation of a plate is parabolic, but for geometric simplicity the deformed shape is approximated by triangles as shown in Figure 7.

$$C_{hydraulic} = -\frac{dV}{dP} \quad (15)$$

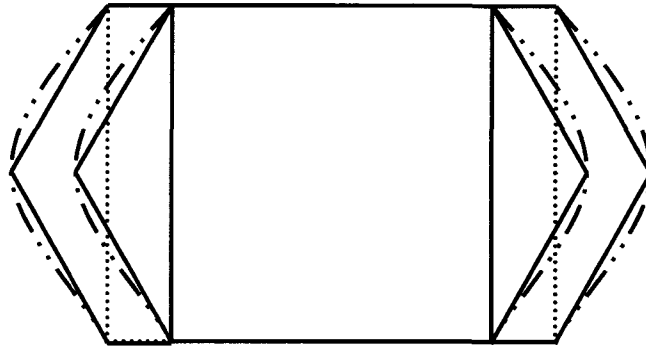


Figure 7 2-D approximation of the membrane deformation, cross-section view

The maximum deformation of a thin rectangular plate occurs at the center of the plate and is given by Equation (16) [77]. In this thin plate model, γ is a geometry factor accounting for the different aspect ratio of the plate, P is the fluidic pressure, h is the

plate height, b is the thickness and E is the modulus of elasticity. In regards to the boundary conditions of the plate, the model assumes that the two long edges of the plates are fixed and two short edges are simply supported. Geometry factor γ can be obtained from fitting an analytical curve to match membrane deformation results from finite-element analyses or experimental measurements. The expanded volume of a single membrane as a function of pressure is shown in Equation (17).

$$x_{\max} = \gamma \frac{P h^4}{E b^3} \quad (16)$$

$$V = \frac{1}{2} h l \gamma \frac{P h^4}{E b^3} \quad (17)$$

The deformation for a microchannel with two in-plane membrane is shown in Equation (18). According to Equation (15), the capacitance is found by differentiation of the volume with respect to pressure, which gives Equation (19). Alternatively, the capacitance of the compliant channel can be characterized with finite-element analysis, followed by fitting a model to the volume increment due to fluidic pressure. A hydraulic capacitor is analogous to an electrical capacitor which stores electric charges when an electrical voltage is applied. The definition of electrical capacitance is given by Equation (20).

$$V = l \gamma \frac{P h^5}{E b^3} \quad (18)$$

$$C_{\text{hydraulic}} = l \gamma \frac{h^5}{E b^3} \quad (19)$$

$$C_{\text{electrical}} = -\frac{dq}{dv} \quad (20)$$

A transient analysis might require consideration of fluidic inertial effects. As a result of fluidic inertia, the acceleration of flowrate might not respond immediately to the transient pressure fluctuations. Therefore, the flowrate might lag the applied pressure. Analogous to electrical inductance, fluidic inertial effects are described as fluidic inductance. If the flow is laminar and the operating frequency is less than the resonance frequency of the flow, the inertial effects can be assumed negligible [47]. This assumption is applied in all subsequent analyses. For completeness, however, fluidic inductance is explained briefly below. Fluidic inductance can be estimated by applying Newton's second law $F=ma$ or the momentum equation to a control volume, yielding Equation (21) [70]. Fluidic inductance is a function of fluidic density ρ , channel length l , channel width w , and channel height h . This is shown in Equation (22) [78]. Comparing Equation (21) and Equation (23), fluidic inductance has a mathematical form that is similar to that of electrical inductance.

$$F = m \frac{dv}{dt}$$

$$\Delta P \cdot \text{Area} = \rho \cdot l \cdot \frac{dQ}{dt} \quad (21)$$

$$\Delta P = \frac{\rho l}{\text{Area}} \frac{dQ}{dt}$$

$$L_{\text{fluidic}} = \frac{\rho l}{wh} \quad (22)$$

$$v = L_{\text{electrical}} \frac{di}{dt} \quad (23)$$

Given the strong resemblance of fluidic and electrical circuits, a fluidic system can be analyzed using electrical simulation tools. Series and parallel combinations of discrete fluidic elements can be used to model a fluidic system. The fluidic circuit model for flow through a section of a compliant membrane microchannel is shown in Figure 8 [65]. The model is scalable to account for multiple membrane pairs or different configurations. The analogy between a fluidic circuit and an electrical circuit is summarized in Table 1.

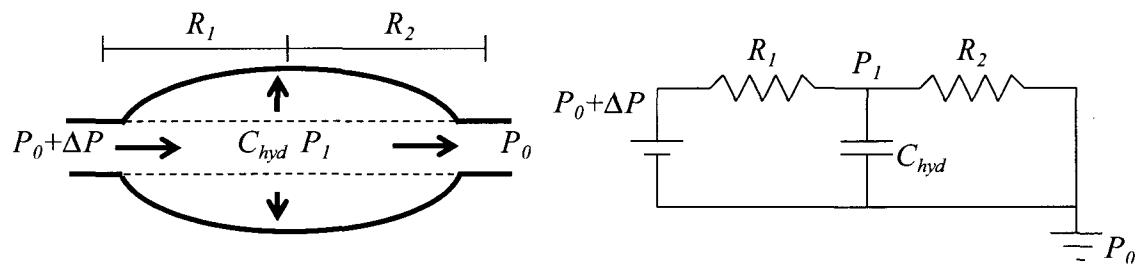


Figure 8 Equivalent circuit modeling of a single unit membrane

Table 1 Summary of fluidic circuit and electrical circuit equivalence

Fluidic Circuit		Electrical Circuit	
Resistance	Pa	Resistance	ohm/ v A ⁻¹
Capacitance	m ³ Pa ⁻¹	Capacitance	farad/ c v-1
Inertia	Pa s ² m ⁻³	Inductance	henry/v s A ⁻¹
Pressure	Pa	Voltage	volt/v
Volume	V	Charge	coulomb/c
Flowrate	m ³ s ⁻¹	Current	ampere/c s-1

3.2 Mechanics of Hyperelastic Materials

The assumptions of linear stress-strain relationship and small deformation in elementary structural mechanics theory are not valid when modeling hyperelastic materials that exhibit large deformations and nonlinear stress-strain relationships. In the case of hyperelastic materials, an alternative constitutive model is required. Examples of hyperelastic materials include butadiene rubber, natural rubber and elastomers. The modeled microfluidic structure is PDMS and it is an elastomeric material. In general, elastomeric materials differ from metallic materials with respect to arrangement of atoms in the microscopic scale. Metals have a crystalline lattice of atoms that is more ordered than elastomeric materials. Conversely, most elastomeric materials have long, cross-linked polymer chains. Compared to other polymers in general, elastomeric materials are exceptionally resilient under loading and are able to return quickly to their original shape upon unloading. Some biological tissues such as artery and bladder tissues, also exhibit hyperelastic behavior and can be modeled with hyperelastic constitutive models [79-81]. A list of widely used hyperelastic constitutive models is summarized in Table 2 [82-85]. The following discussion will focus on the Mooney-Rivlin hyperelastic model.

Table 2 Summary of hyperelastic models categorized according derivation origins

Model Classification	Hyperelastic Model
Phenomenological model	Polynomial model, Mooney-Rivlin model, Ogden model, Yeoh model
Mechanistic model	Arruda-Boyce model, Neo-Hookean
Phenomenological and mechanistic hybrid model	Gent model

PDMS exhibits a nonlinear stress-strain relationship that can be modeled with the Mooney-Rivlin hyperelastic constitutive model. The Mooney-Rivlin constitutive model is very robust and the model is scalable to account for higher order nonlinearities. Modeling PDMS with a Mooney-Rivlin approach has excellent agreement with experimental results [38, 84]. Yu et al. studied a PDMS based membrane and microcantilever beam with Mooney-Rivlin and linear elastic models [84]. Results showed that for a strain larger than 4%, a linear elastic model yields more than 10% error. When modeling a part with large strain, the Mooney-Rivlin hyperelastic model is more appropriate.

The Mooney-Rivlin hyperelastic model is based on strain energy methods with the assumption that the material is isotropic and incompressible. The basic strain energy of a Mooney-Rivlin constitutive model is given by Equation (24). The finite-element software, COMSOL Multiphysics (COMSOL Inc., Burlington, MA, USA) implements the strain energy in the form of Equation (25) [85-87]. I_n is the invariant, C_{10} and C_{01} are material parameters, K is the bulk modulus, and J_{el} is the elastic volume ratio. Mooney-Rivlin parameters C_{10} and C_{01} , are obtained from the regression of stress-strain test data. The parameters may be non-unique as long as they sufficiently fit the material test data [88]. Although the COMSOL Multiphysics software natively supports 2-parameter Mooney-Rivlin, it is also possible to modify the strain energy equation to handle additional Mooney-Rivlin parameters that account for higher order nonlinearities [88]. Shown in Equation (26) is a 9-parameter strain energy equation. Another natively

supported constitutive model, the Neo-Hookean model is a simple single-parameter form of the Mooney-Rivlin model.

$$W_s = C_{10}(\bar{I}_1 - 3) + C_{01}(\bar{I}_2 - 3) \quad (24)$$

$$W_s = C_{10}(\bar{I}_1 - 3) + C_{01}(\bar{I}_2 - 3) - p(J_{el} - 1) - \frac{p^2}{2K} \quad (25)$$

$$\begin{aligned} W_s = & C_{10}(\bar{I}_1 - 3) + C_{01}(\bar{I}_2 - 3) + C_{20}(\bar{I}_1 - 3)^2 + C_{11}(\bar{I}_1 - 3)(\bar{I}_2 - 3) \\ & + C_{02}(\bar{I}_2 - 3)^2 + C_{30}(\bar{I}_1 - 3)^3 + C_{21}(\bar{I}_1 - 3)^2(\bar{I}_2 - 3) + C_{12}(\bar{I}_1 - 3)(\bar{I}_2 - 3)^2 \\ & + C_{03}(\bar{I}_2 - 3)^3 - p(J_{el} - 1) - \frac{p^2}{2K} \end{aligned} \quad (26)$$

The bulk modulus K is estimated by Equation (27) for homogeneous isotropic materials. Young's modulus can be estimated from the fitted Mooney-Rivlin parameters with Equation (28) [88]. Substitution of the estimated Young's modulus gives the bulk modulus of a hyperelastic material, shown in Equation (29) [89].

$$K = \frac{E}{3(1 - 2\nu)} \quad (27)$$

$$E = 6(C_{10} + C_{01}) \quad (28)$$

$$K = \frac{2(C_{10} + C_{01})}{(1 - 2\nu)} \quad (29)$$

For modeling purposes, the hyperelastic material properties of 10:1 curing ratio Sylgard 184 PDMS (Dow Corning Corp., Midland, Michigan, USA) was acquired through contract testing service from Datapoint Labs (Ithaca, New York, USA). A 2-parameter Mooney-Rivlin model was extracted by least-squares nonlinear regression from the stress-strain test data. The first (C_{10}) and second (C_{01}) Mooney-Rivlin constants were

determined to be 0.230 MPa and 0.204 MPa respectively. The fitted curve is plotted against experiment data in Figure 9 and Figure 10. Elastomeric materials such as PDMS are essentially incompressible and the Poisson's ratio is assumed to be 0.49 in order to satisfy the bulk modulus equation. The PDMS density is assumed to be 1027.94 kg/m³.

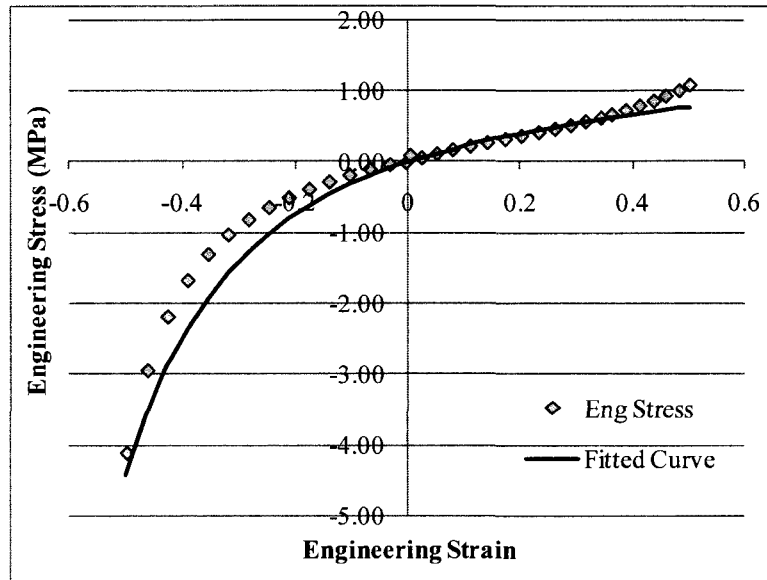


Figure 9 Fitted Mooney-Rivlin planar stress-strain curve to measured stress

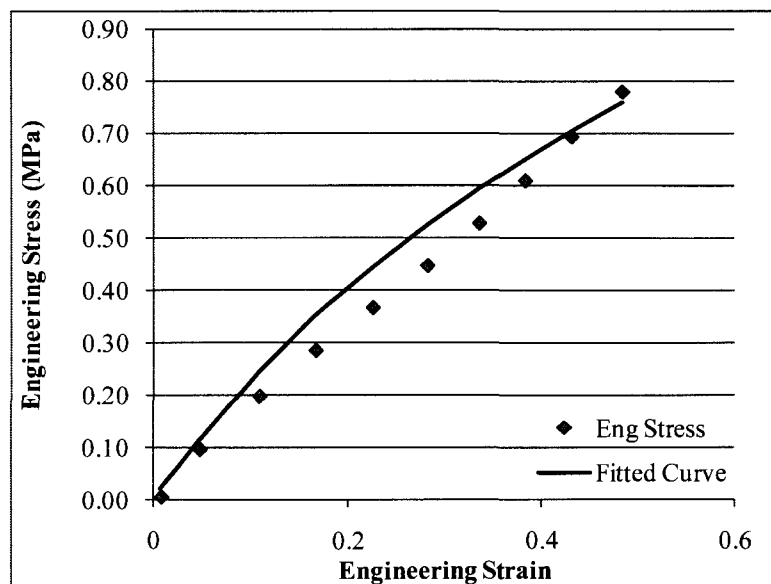


Figure 10 Fitted Mooney-Rivlin uniaxial stress strain curve to measured stress

3.3 Numerical Simulation

Numerical simulation of attenuation of pulsatile flow was done through a finite-element analysis using COMSOL Multiphysics. The finite-element analysis of a fluid-structure interaction problem consists of coupled physical domains. First, a fluid-mechanics analysis is required to solve for the pressure distribution and flow velocity in the microchannel. Second, structural-mechanics analysis of the microchannel wall deformation due to fluidic pressure and viscous force is required to solve for the expansion of microchannel. The deformation of the microchannel wall increases the overall fluidic volume present in the microchannel and decreases the exit flowrate simultaneously. A 2-way coupling of fluid mechanics and structural mechanics is required to reveal the dampening effects. The coupling of both physical domains involves deforming geometries and moving boundaries which requires a moving mesh interface. The moving mesh interface is handled through an Arbitrary Lagrangian-Eulerian (ALE) approach which will be discussed in Section 3.3.1. The entrance length is also determined in Section 3.3.2 and is set such that the flowrate is acquired at a fully developed region. The simulation setup and boundary conditions will be discussed in Section 3.3.3.

3.3.1 Arbitrary Lagrangian-Eulerian (ALE)

An Arbitrary Lagrangian-Eulerian (ALE) frame is a combined kinematic description of Lagrangian and Eulerian representations. It was first used in fluid mechanics simulation and has been successfully used in multiphysics problems such as magnetohydrodynamics and electrostatic induced structural deformation [90].

Implementing ALE becomes an important consideration, when the simulated continuum experiences strong distortions or structural deformation that can affect the results of other associated simulated physical domains. This section will provide a brief introduction to ALE moving mesh based on works of Donea et al. [91] and Zienkiewicz et al. [92].

A Lagrangian description is largely used in solving structural-mechanics problems. It establishes a mesh to the object and each individual node tracks the deformation position. ALE can be applied to both static and transient analyses. For transient analyses, each node and its associated deformation position is tracked at each time step. Conservation of mass is preserved since the mesh always contains same amount of mass. An advantage of using the Lagrangian description is that the problem has no convective acceleration and is self-adjoint, therefore mathematically easier to solve. However, using a Lagrangian description in complex motions such as vortices in fluid mechanics causes severe mesh deformation and is thus unsuitable.

Fluid mechanics problems are often better addressed using an Eulerian description, for which the boundaries of the fluid motion and the computational mesh are fixed in position. As time steps progress, fluid particles are monitored through the fixed boundaries. Generally, the recorded velocity and pressure values are the instantaneous quantities at the mesh node or boundary without referencing to the initial particle location. The conservation of mass is accounted for by the equilibrium of the net flow flux through each mesh node. The dissociation of the mesh nodes and the fluid particle causes convective effects because of relative motion between moving particle and mesh

node. Furthermore, computational issues arise for free surface and moving fluidic boundary problems when the position of the boundary is not a known condition.

The shortcomings of traditional Lagrangian and Eulerian descriptions give rise to an intermediate description that combines the advantages of these traditional descriptions known as the Arbitrary Lagrangian-Eulerian (ALE) description. The ALE method implements a third set of reference coordinates to map the structural mesh deformation to the fluidic mesh deformation. In the fluid-structure simulation of deformable membranes, the Navier-Stokes equations are solved for the fluid dynamics properties, including pressure and fluid velocity, which will deform the membranes. Then, the structural-mechanics computation solves for the deformation which provides wall displacement and velocity boundary conditions for the fluid mechanics and ALE mesh. The ALE mesh updates the deformation of the fluidic mesh which is prescribed by the displacement and velocity of the membrane structural mechanics, followed by reformulating the Navier-Stokes equations to solve for the flow condition. This mesh-updating algorithm is known as the ALE moving mesh.

In COMSOL Multiphysics, the fluidic domain is tied to the ALE moving mesh, and the fluidic partial differential equations are transformed by taking the structural deformation and moving boundaries into account. At the interface of structural mechanics and fluid mechanics, displacement and velocity continuity is enforced. In other words, the displacement of any node in the structure is equal to the displacement of a fluid particle at that node, and the velocity of any node in the structure is equal to the velocity of a fluid particle at that node. Implementation of the moving mesh also requires

mesh regulation such that the mesh remains appropriate to the system. By default, COMSOL uses the Winslow smoothing technique to reduce excessive mesh distortion or to avoid an inverted mesh problem [87]. In cases for which the mesh is severely deformed, it is possible to prescribe a quality parameter of the deformed mesh as a stop condition in the solver. This provides an opportunity to remesh the deformed geometry before solving the next iteration.

3.3.2 Entrance Length

Before constructing the simulation geometry, the entrance length of fluid flow is determined and accounted for in the simulation geometry. The velocity measurement point and flowrate measurement boundary is then located within the fully developed region to ensure consistency. Dimensional analysis is used to relate the Reynold's number Re to the entrance length l and conduit diameter d , as shown in Equation (30) [70]. An alternative entrance length for a rectangular microchannel is given by Equation (31) [93]. It is reported that when the aspect ratio of a square microchannel, $h/w = 1$, the entrance length is close to a circular channel [94]. A summary of the calculated entrance length in microns is shown in Table 3. The entrance flowrate measurement is made at least $35 \mu\text{m}$ after the inlet to ensure the inviscid boundary layers merge and a fully developed inlet flowrate is measured.

$$\frac{L_e}{d} \approx 0.06 Re \quad (30)$$

$$\frac{L_e}{h} \approx \left(-0.129 \left(\frac{h}{w} \right)^2 + 0.157 \frac{h}{w} + 0.016 \frac{h}{w} \right) Re \quad (31)$$

Table 3 Entrance length of different flowrate

Entrance Length (μm)	Flowrate ($\mu\text{L}/\text{min}$)		
	10	20	30
Circular with Hydraulic Diameter	10.0	20.0	30.0
Rectangular	7.3	14.7	22.0

3.3.3 Simulation Model Definition and Boundary Condition

The FSI model simulates two different compliance levels of microchannels with a step and a sinusoidal pressure inlet conditions. The 2-way coupling and ALE moving mesh are performed with the COMSOL Multiphysics predefined FSI analysis. The simulation is conducted in 2-D to focus on the general effects of compliance on pulsatile flow damping, without the high computational demands of a full 3-D model. The cross section and length of the experimental test device is $40\ \mu\text{m} \times 40\ \mu\text{m} \times 40\ \text{mm}$. The geometry is relative long compared to its cross section, thus a full-model simulation is unfeasible. Furthermore, the fluidic domain of the simulation would require sufficiently dense meshing to accurately track the expanded fluidic volume and predict flow stabilization. The 2-D simulation is used to predict the pulsatile stabilization trend and how flow velocity and pressure change with compliance. The more compliant microchannel is approximated by a $120\ \mu\text{m}$ thick structure which represents a thin membrane microchannel. On the other hand, the less compliant microchannel is approximated by a $240\ \mu\text{m}$ thick structure which represents a solid thick wall microchannel. The simulated microchannels consisted of four 2 mm long membrane pairs, as shown in Figure 11.

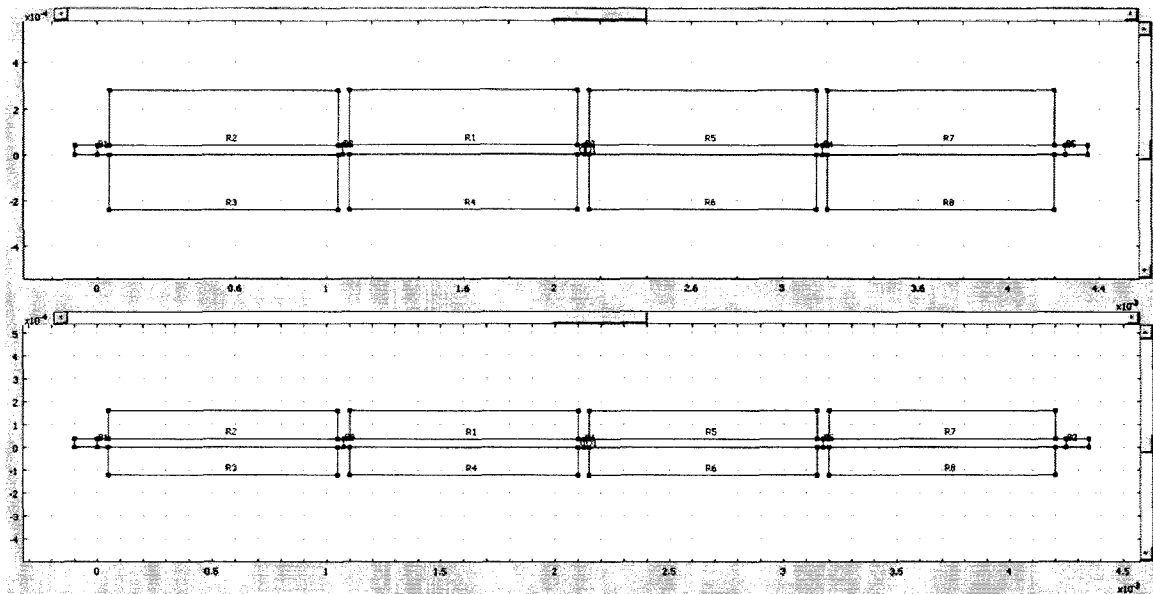


Figure 11 COMSOL Multiphysics geometry of simulated plain microchannel (top) and simulated membrane microchannel (bottom) for comparative simulation

The FSI simulation consists of plane-strain structural mechanics and incompressible Navier-Stokes flow which are both tied to an ALE moving mesh. In the structural plane-strain mode, large deformation and Mooney-Rivlin hyperelastic material behavior are considered. The simulated fluid is assumed to be standard deionized water with a fluid viscosity of 0.001 Pa·s and density of 1000 kg/m³. The hyperelastic material model is implemented as discussed in Section 3.2. Since the simulated problem is a transient analysis, a time marching algorithm is used to solve the problem. The algorithm is based on the differential-algebraic equation solver (DASPK), which uses a variable order and variable step-size back differentiation formula [87]. It is an implicit solver and hence an inherently stable algorithm [95]. The solver also requires sufficiently fine relative and absolute tolerances to obtain accurate results. The tolerance is set to 1x10⁻⁶ for relative tolerance and 1x10⁻⁷ for absolute tolerance. Quadrilateral elements are used

to mesh the geometry according to a mapped meshing feature in the FEA software to control element size and the distribution of the mesh nodes.

To simulate a step inlet pressure, a smoothed Heaviside function with a continuous second-derivative inlet pressure is used. The Heaviside function provides a smooth and continuous inlet condition which is required by the numerical solver to achieve convergence. During a step change for a real physical system, the dynamics are also expected to deviate from an idealized step change because of fluidic inertia, microbubbles, and compliant fluidic components present in the fluidic system. The step interval is set to 1ms with an inlet pressure of 1.8 kPa which approximates an instantaneous pressure rise. For the sinusoidal pressure simulation, the input pressure is constructed with a piecewise analytical function that is composed of series of sinusoidal frequencies at 2, 4 and 6 Hz. The input boundary conditions are provided in Table 5. Note that "flc2hs" is the representation of smoothed Heaviside function in COMSOL Multiphysics. The outlet pressure is assumed to be atmospheric and is thus set to a pressure value of zero. In the fluidic domain, the membrane wall fluidic interface boundary is set to "structural velocity." This is to maintain velocity continuity between the fluid and moving wall. Any non-moving wall sections are treated with a no-slip boundary condition, representing viscous shear at the wall. In the structural mechanic domain, the interface between the deformable microchannel walls and fluidic domain is set to fluid load which is given by Equation (32) [87]. " \mathbf{I} " is the unit diagonal matrix and " \mathbf{n} " indicates a vector that is normal to the boundary. The load is the sum of the normal force vector due to fluidic pressure and fluidic viscous shear forces along the boundary.

The intermediate section between each membrane is assumed to be non-deforming. As a result, both the left and right ends of each membrane are set to a fixed boundary condition.

$$\mathbf{F}_T = -\mathbf{n} \cdot \left[-p \mathbf{I} + \mathbf{v}(\nabla \mathbf{u} + (\nabla \mathbf{u})^T) \right] \quad (32)$$

In the ALE moving mesh domain, the moving boundaries between the deformable microchannel walls and fluidic interface are set to “structural displacement”. The non-moving fluidic wall boundaries are set to “fixed”. The boundary conditions used in the simulation are summarized in Table 4. All boundary conditions for step and sinusoidal pressure simulations remain the same with the exception of the inlet condition.

Table 4 A summary of simulation boundary condition. Non-specified conditions remain the default settings in COMSOL Multiphysics.

Simulation Domain	Selected Boundary	Boundary Condition
Plane strain boundary (Active solid domain)	Membrane wall Non-deformable wall	Fluid load Fixed
ALE boundary (Active fluid domain)	Membrane Wall Remaining boundaries	Structural displacement Fixed
Incompressible Navier- Stokes (Active fluid domain)	Inlet Outlet Membrane wall	Pressure, No viscous stress Zero Pressure, no viscous stress Structural velocity

Table 5 Time dependent pressure condition at the inlet of the microchannel. Left, step input pressure. Right, 2, 4, 6 Hz sinusoidal pressure wave with specified time step

Step Pressure	Sinusoidal Pressure	
	Time	Pressure
$1800 \cdot \text{Flc2hs}(t-0.001,0.001)$	0	1600 Pa
	0.2	$1600 \text{ Pa} \cdot (1+0.2 \cdot \sin(2 \cdot \pi \cdot 2 \cdot (t-0.2)))$
	1.2	$1600 \text{ Pa} \cdot (1+0.2 \cdot \sin(2 \cdot \pi \cdot 4 \cdot (t-1.2)))$
	1.7	$1600 \text{ Pa} \cdot (1+0.2 \cdot \sin(2 \cdot \pi \cdot 4 \cdot (t-1.7)))$

Chapter 4 Experimental Methods

4.1 Microfluidic Chip Fabrication

The microfluidic chip was fabricated with a soft-lithography casting technique. The mold was fabricated with a single layer SU-8 (SU-8 2035, MicroChem Corp., Newton, MA) photolithography process [96]. A photomask is required for the photolithography process. The photomask is a negative image of the geometry of the microfluidic chip which can include wells, microchannels and thin-walled structure. The photomask was drafted using AutoCAD software (Autodesk, Inc., San Rafael, California, USA). The layout of the mask is shown in Figure 12. The 1 mm and 2 mm rectangular block in the mask layout are the air cavities of the microchannel membrane. The photomask can be fabricated on glass, quartz, or mylar substrates. In this study, the mask was fabricated by laser photoplotting onto a 175 μm mylar film with 20,000 dots-per-inch (DPI) resolution, by CAD/Art Services, Inc (Bandon, Oregon, USA).

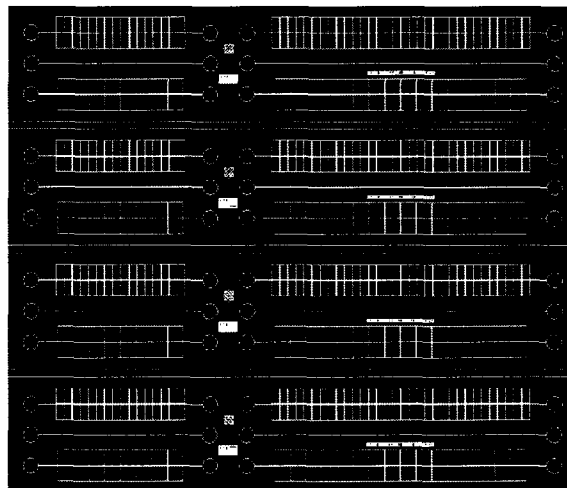


Figure 12 Layout of photo mask. Left, 20 mm microchannel. Right 40 mm microchannel. Mask contains 4 replicates of similar channel configuration.

The mold fabrication started with preparing a silicon wafer substrate by Piranha cleaning (sulfuric acid and hydrogen peroxide mixture) to remove organic contaminants. This step was followed by dehydrating the substrate at 150 °C for 10 min on a hotplate. After loading the cleaned substrate into a photoresist spin coater, the wafer was spun to remove dust particles. Next, the substrate was spun with SU-8 2035 photoresist at 500 rpm for 15 s which transitioned into 2500 rpm for 40 s. These spin settings should result in a 40 μm thick layer of SU-8 [97]. The SU-8 spun wafer was soft-baked for 3 min at a 65 °C on a hotplate. The wafer was then transferred to a 95 °C hotplate and baked for 9 min. The soft-baked substrate was then exposed to a UV light source using a Quintel Q4000 contact aligner (Neutronix, Inc., Santa Ana, California, USA) under a high resolution laser printed photomask. A UV filter that eliminated radiation below 350 nm wavelength was used to ensure the fabricated sidewalls of the SU-8 mold were vertical [2]. Similar to the soft-bake process, the exposed SU-8 wafer was post-baked for 3 min at 65 °C followed by 9 min at 95 °C in a two step process. After baking, the wafer was removed from the hotplate and allowed to cool down to room temperature for a few minutes. The cooled wafer was then developed in a SU-8 developer solution (MicroChem Corp., Newton, MA) for approximately 7 min followed by drying with compressed air. The completed SU-8 mold is shown in Figure 13. A cross section profile of a fabricated SU-8 region was imaged using a Wyko NT9100 optical profiler (Veeco Instruments Inc., Plainview, New York, USA) and is shown in Figure 14. The actual fabricated height was approximately 34 μm and the membrane cavity was 13.87 μm wide. During the fabrication of the SU-8 mold, many issues were faced such as poor

photolithographic resolution and the delamination and cracking of SU-8 structures. A SU-8 optimization study was performed to refine the process and the details of this study can be found in Appendix I.

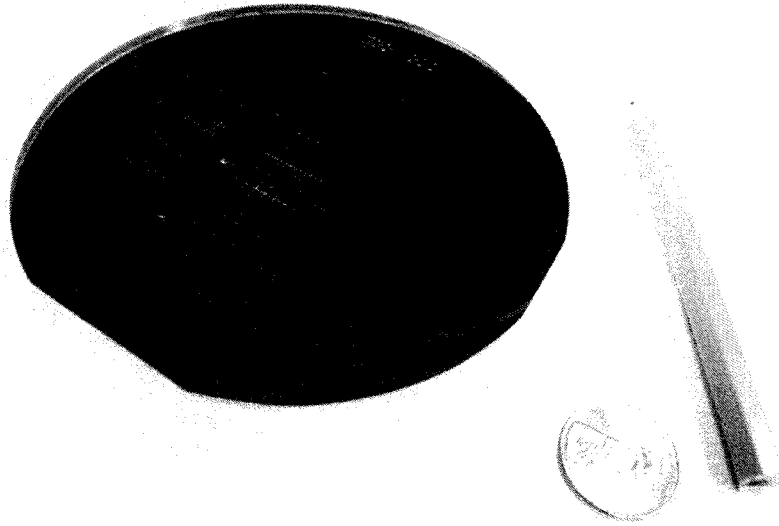


Figure 13 Fabricated SU-8 based mold structure on silicon wafer

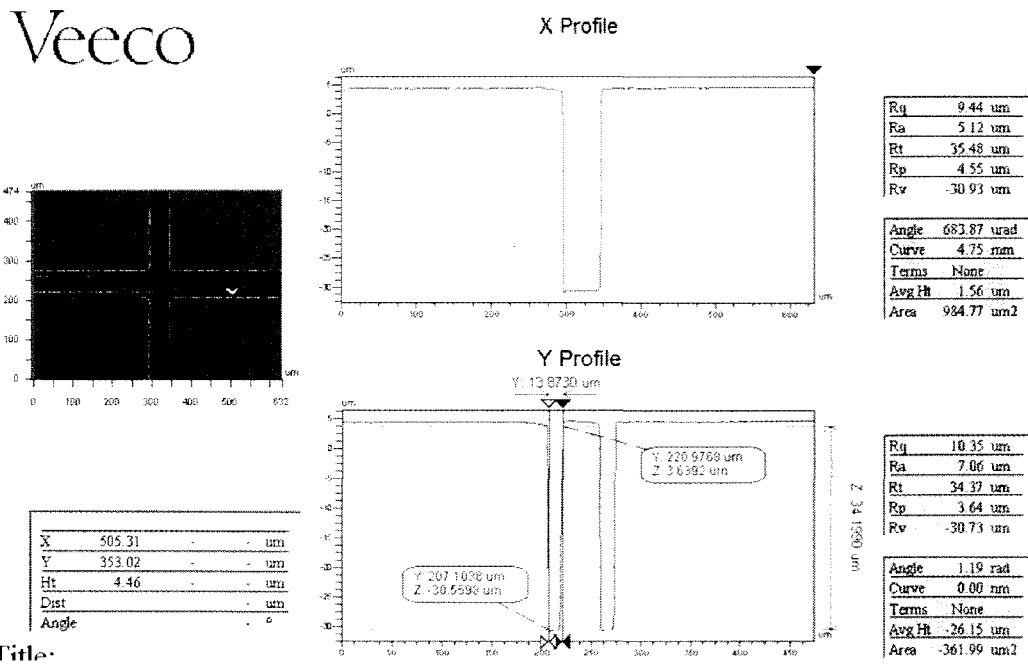


Figure 14 Cross section of a SU-8 membrane microchannel mold.

After the SU-8 mold was fabricated, the molding surface was treated with a few drops of triridecafluorooctyltrichlorosilane (T2492 from United Chemical Technologies, Inc., Bristol, Pennsylvania, USA) and held under vacuum for 30 min. This treatment allows for easy release of the cured PDMS samples from the SU-8 mold. The PDMS polymer was prepared by thoroughly mixing the PDMS pre-polymer and curing agent in a ratio of 10:1 by weight. The mixture was degassed under vacuum in a desiccator to remove air bubbles in the mixture. Then the mixture was poured onto a SU-8 mold and cured at 150°C for 20 min. Once the PDMS was cured, the PDMS casting was peeled from the mold and each microfluidic chip was diced to size.

Prior to bonding, a sharp syringe tip was used to core the connection ports to the microchannel. To remove dust particles, the PDMS chips were cleaned with an adhesive tape and isopropanol. Oxygen plasma surface treatment was performed on the PDMS chips and 25 mm x 75 mm microscope glass slides in a Harrick Plasma PDC-001 plasma cleaner (Model, Harrick Plasma, Ithaca, New York, USA). The oxygen flowrate was set to 9 sccm and the plasma chamber pressure was allowed to reach 500 mTorr steady state pressure before initiating the plasma reaction. The plasma power was set to 6.8 watts (low) and the PDMS chip and glass substrate were exposed to oxygen plasma for 20 seconds. Subsequently, the treated surfaces of the PDMS chips and glass substrates were brought into contact and a Teflon rod was rolled over the PDMS chips to drive out trapped bubbles between mating surfaces. The bonded chips were placed on a 65°C hotplate for 1 minute.

The manufactured microfluidic chip required consistent fluidic connection between a fluidic pressure source and the microfluidic chip for a successful fluidic experiment. The fluidic connection was provided by a length of Upchurch Scientific 1569 hard polymer tubing (Upchurch Scientific, Oak Harbor, Washington, USA) which was inserted into each cored holes of the microfluidic chip. The end of each tube was cut at a 45° angle to ease insertion into the cored hole. A 3 mm thick, ring shaped PDMS piece was cut and placed around the base of the tubes. Liquid PDMS was poured into the precut PDMS ring and subsequently cured. This formed a leak free seal on the interface between the tubes and the microfluidic chip. This method provided a reliable and stress-free fluidic connection.

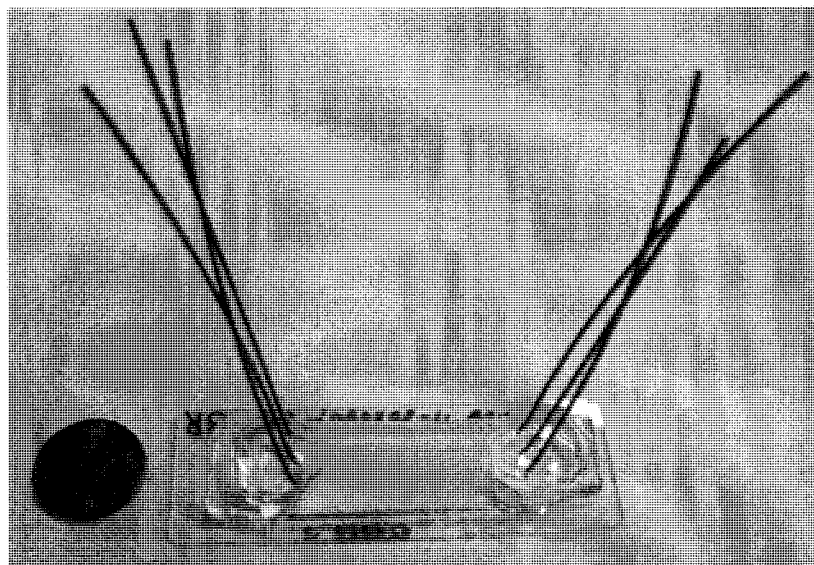


Figure 15 A microfluidic test chip attached with polymer tubing compared to a US penny.

4.2 Experimental Plan and Procedures

The experimental objectives were to characterize the compliance of the microchannels and to measure its relative effectiveness as pulsatile pressure damping devices. The experimental setup diagram and details is as shown in Figure 16 and Table 6 respectively. The fluidic driving source was a regulated compressed air tank connected to a laboratory pressure bottle filled with deionized water. The fluid exiting the pressure bottle entered a silicon tube which then entered a 4-way flow valve. The silicon tube passed through a solenoid pinch valve which can be triggered to compress the silicon tube. The solenoid pinch valve was control signal was provided by a function generator. When the solenoid provided a series of compressing action, it abruptly reduced and increased the flowrate, producing a pulsatile flow. Since the function generator is unable to supply sufficient current to the pinch valve, a DC-to-DC relay and an external power supply was used to amplify the signal. The operating principle of the DC-to-DC relay behaves like an on-off switch, thus producing a square like pulsatile wave. The 4-way valve was used to produce a step pressure input to the system. One of the connections on the valve was plugged in order to make it function as a 3-way valve. In this configuration, the valve would permit only one-way fluidic flow path. The 4-way valve was submerged in a water-filled container to prevent introduction of air bubbles when the fluidic line was open to zero gage pressure. The flow characteristics were quantified by two pressure sensors, P_1 on the inlet side and P_2 on the outlet side. The analog voltage of the pressure sensors were recorded through a data acquisition board attached to a computer. The output voltage of the each pressure sensor is proportional to the

corresponding line pressure to which it is subjected. The end of the outlet tube was submerged in a shallow waste reservoir to prevent bubble formation and evaporation of fluid in the tube. The relatively slow sampling frequency of the flowmeter was unable to capture the dynamics of tested pulsatile flow. As a result, it was not used to quantify flowrate dynamically, but rather just to check for flow consistency. The actual test hardware is shown in Figure 17.

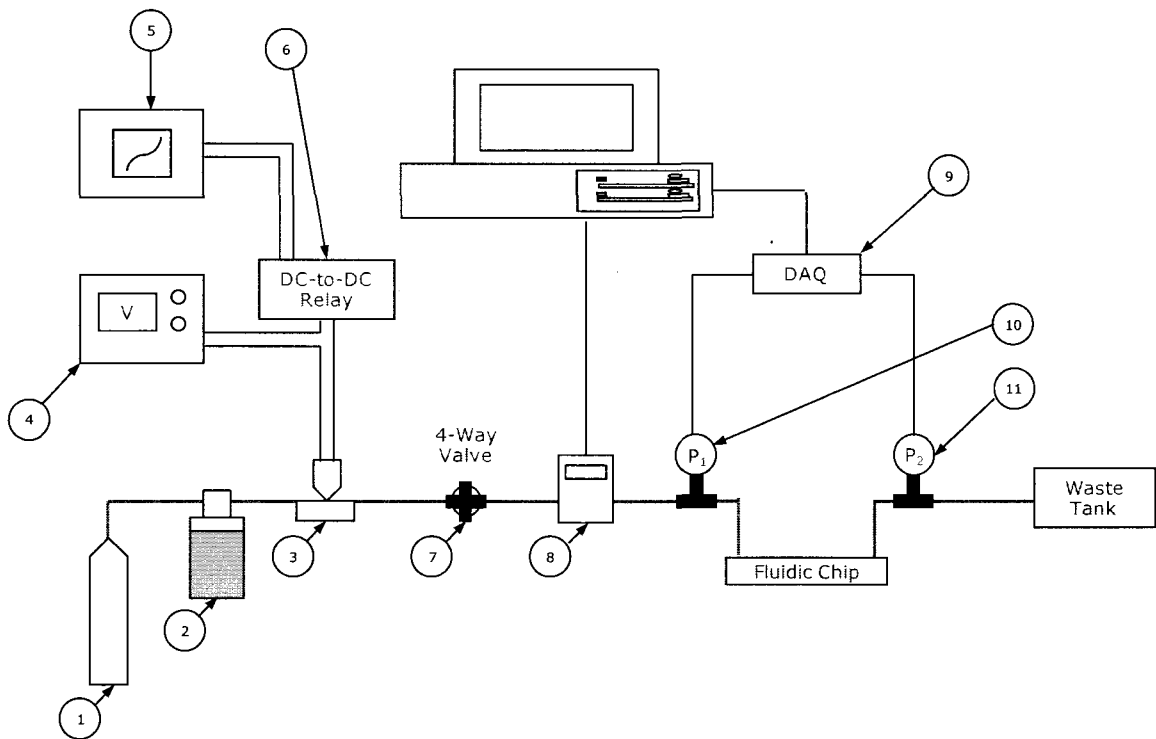


Figure 16 Diagram of the fluidic control and measurement system.

Table 6 Bill of material of the fluidic control and measurement system

Item	Description/Part Number	Manufacturer	Part Number
1	Compressed Air	Praxair, Danbury, Connecticut, USA	-
2	500 ml Laboratory Bottle	SCHOTT North America, Inc., Elmsford, New York, USA	GL 45
3	Pinch Valve	ASCO, Florham Park, New Jersey, USA	H284A011SCPD1
4	Power Supply	BK Precision, Yorba Linda, California, USA	1670A
5	Function Generator	BK Precision, Yorba Linda, California, USA	4017A
6	DC-to-DC Relay	Crydom, San Diego, California, USA	D2D12L
7	4-Way Valve, 3-port Flow	Upchurch Scientific, Oak Harbor, Washington, USA	V-101T
8	Flowmeter	Upchurch Scientific, Oak Harbor, Washington, USA	N-565
9	Data Acquisition Device	National Instruments, Austin, Texas, USA	NI USB-6009
10	Pressure Sensor	Honeywell Sensing and Control, Golden Valley, Minnesota USA	40PC015G1A
11	Pressure Sensor	Honeywell Sensing and Control, Golden Valley, Minnesota USA	40PC001B1A

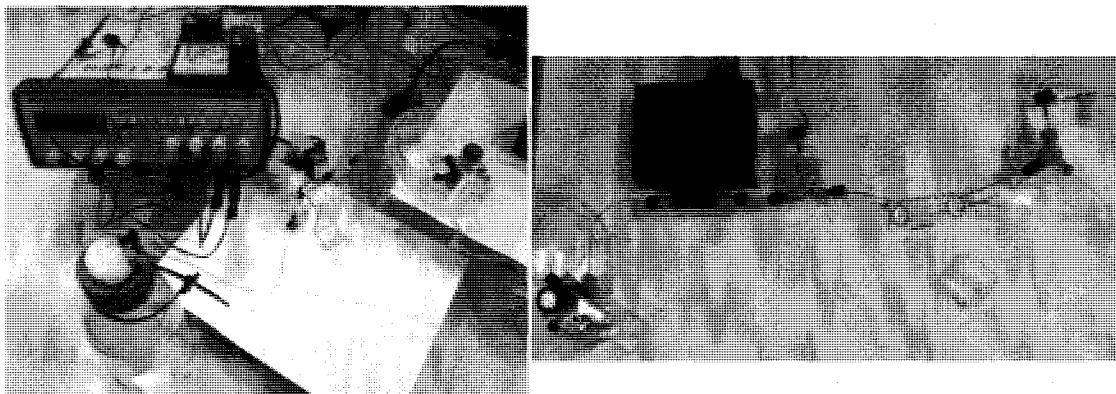


Figure 17 Actual fluidic control and measurement hardware

The compliance of the plain and membrane microchannels were characterized by a step-pressure input condition. Before beginning the test, the 4-way valve was initially turned to the pressurize water line to fill the microchannel until the flow was steady. The channel was then vented to atmospheric pressure. While recording the pressure data at 100 Hz, the 4-way valve was quickly turned to the pressurized line to produce a step pressure input. The inlet rise pressure was used to characterize the compliance of the microchannel. The pulsatile flow damping abilities of each microchannel were

characterized through a series of 2, 4 and 6 Hz pulsatile-pressure input condition. The inlet and outlet pressure fluctuation was then used to compare the relative pulsatile pressure damping ability between each microchannel configuration. For consistency, the measurements were performed with the same pressure and pulsatile frequency condition for all microchannel configuration.

4.3 Uncertainty Analysis

Any measurement equipment inherently contains some level of uncertainties due to random variation in measurement data and random equipment consistency. Since measurement uncertainties affect the validity of measured data, these uncertainties are investigated. The uncertainty analysis can be classified into two categories, systematic and random uncertainty [98]. Systematic uncertainty is the natural equipment errors and is usually provided by the equipment manufacturer. Linearity and hysteresis error are sources of systematic uncertainty. Random uncertainty is the chance measurement errors such as repeatability, thermal stability and quantization error. The uncertainty specifications for pressure sensor P_1 (103421 Pa pressure sensor) and P_2 (6665 Pa pressure sensor) are given by the manufacturer and are listed in Table 7. The combined root sum of square (RSS) systematic uncertainties are 2.03% and 2.30% full span for pressure sensor P_1 and P_2 respectively. Since the pressure sensors are connected through an analog-to-digital data acquisition device, its uncertainty also needs to be considered. The absolute accuracy of the 14-bit NI USB-6009 data acquisition device is 4.28 mV at ± 5 V full scale differential measurement. To account for the random uncertainty, a trial experiment run was done on 3 similar microchannels, accounting for run-to-run

variability, channel-to-channel variability and fluidic attachment variability. The pooled standard deviations of each sensor are found to be 262 Pa and 92 Pa for P_1 and P_2 respectively. The combined uncertainties of the pressure sensors and data acquisition device are ± 2133 Pa for P_1 and ± 199 Pa for P_2 , as shown in Table 8.

Table 7 Uncertainty specification of pressure sensors in percentage full span

	Pressure Sensor 1 (Inlet) 0-103421 Pa (15 psi)	Pressure Sensor 2 (Outlet) 0-6665 Pa (50 mmHg)
Null and Span Shift	2.00%	2.12%
Linearity	0.20%	0.80%
Hysteresis	0.15%	0.15%
Ratiometricity	0.25%	0.25%
Combined Pressure Uncertainty (RSS)	2.03%	2.30%

Table 8 Summary of pressure sensor uncertainty

	P_1	P_2
Systematic Uncertainty	2100 Pa	152 Pa
Random Uncertainty	262 Pa	92 Pa
Total Uncertainty	2133 Pa	199 Pa

Chapter 5 Results and Discussion

5.1 Experiment Results and Discussion

5.1.1 Step Pressure Results

As mentioned in the experimental setup, a step pressure input was introduced to both a plain microchannel and a 2 mm membrane microchannel. The microchannels were both 40 mm long. The recorded pressure rise in Figure 18 shows that the more compliant membrane microchannel requires a longer time to reach steady state due to expanding and filling the larger volume. The inlet pressure measurements have an uncertainty of 2.1 kPa, but the difference in pressure rise is still distinguishable. These responses approximate over-damped first-order systems and their rise times can be extracted [99]. The rise time, t_r is the required time for the response to rise from 10% to 90% of the setpoint when subjected to a step input. The extracted values are shown in Table 9. Since the response of a compliant conduit to an applied step pressure input is similar to the response of a resistor–capacitor (RC) low-pass filter to an applied step voltage input, the cutoff frequency of a fluidic system can also be quantified from its step pressure response [47]. The cutoff frequency, f_c is the frequency at which the response is 3 dB less than the zero-frequency value on a Bode plot. In other words, for a pulsatile input wave that is below the cutoff frequency, the output amplitude will be relatively unchanged. Conversely, the outlet amplitude of the pulsatile wave will be attenuated significantly if the pulsatile frequency is above the cutoff frequency. The cutoff

frequency can be estimated with Equation (33). The estimation from the step pressure experiment is shown in Table 9 [47].

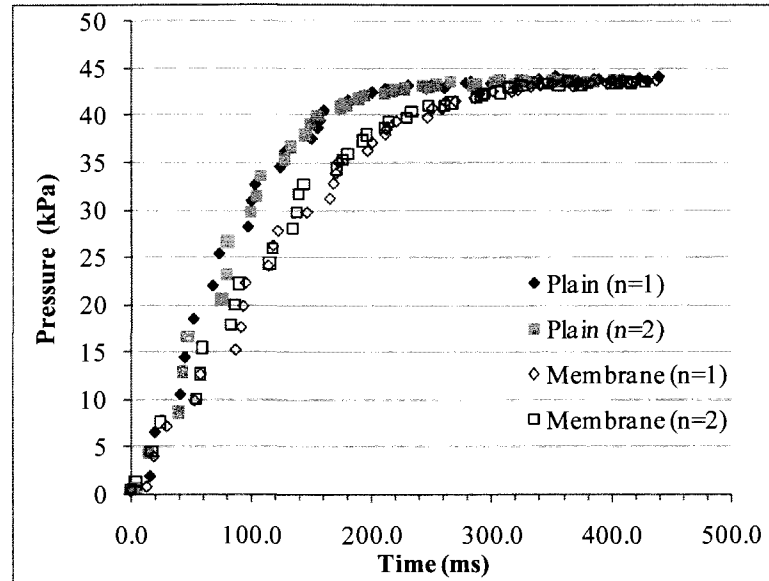


Figure 18 Step rise of a plain and 2 mm membrane microchannel (40 mm). Each microchannel was run with 2 replicates.

$$f_c = \frac{1}{2\pi RC} = \frac{0.35}{t_r} \quad (33)$$

The hydraulic resistances of a plain microchannel and a 2 mm membrane microchannel were also measured during steady state flow, as shown in Table 10. The resistance values were obtained by dividing the steady state pressure by the steady state flowrate. When the measurements were taken, the microchannels were pressurized and were in a fully expanded state. The membrane microchannel has a more compliant wall structure, causing greater cross-sectional expansion than a plain microchannel. Since hydraulic resistance has a fourth-power dependence on the cross-sectional length scale, a membrane microchannel has a lower hydraulic resistance than a plain microchannel, as shown in Table 10. The lower hydraulic resistance is expected to increase the outlet

pressure. The measured hydraulic resistance can then be used in Equation (33) to estimate capacitance. The estimated capacitance is shown in Table 10. The membrane microchannel has a higher estimated capacitance value of $2.19 \times 10^{-16} \text{ m}^3/\text{Pa}$ when compared to plain microchannel capacitance of $1.37 \times 10^{-16} \text{ m}^3/\text{Pa}$. Since cutoff frequency is dependent on hydraulic resistance and hydraulic capacitance, it is interesting to note that a membrane microchannel offers approximately 60% higher hydraulic capacitance and 10% less hydraulic resistance than a plain microchannel.

Table 9 Extracted rise time and cutoff frequency from Figure 18

	Plain Microchannel	2 mm Membrane Microchannel
n=1	137 ms	201 ms
n=2	141 ms	197 ms
Average Rise Time	139 ms	199 ms
Cutoff Frequency	2.52 Hz	1.76 Hz

Table 10 Measured resistance and estimated capacitance of a 40 mm microchannel

	Plain Microchannel	2 mm Membrane Microchannel
Resistance (Measured)	$4.614 \times 10^{14} \text{ Pa s/m}^3$	$4.13 \times 10^{14} \text{ Pa s/m}^3$
Capacitance (Estimated)	$1.37 \times 10^{-16} \text{ m}^3/\text{Pa}$	$2.19 \times 10^{-16} \text{ m}^3/\text{Pa}$

5.1.2 Pulsatile-Wave Results

A plain microchannel and a membrane microchannel were subjected to a pulsatile inlet pressure as detailed in the experimental setup. The pulsatility of a pressure wave was quantified by the root mean square (RMS) average of the pulsatile pressure. RMS average represents the standard deviation with its mean removed or simply the pulsatile component of the wave. This indicator is widely used in the analysis of alternating current (AC) circuits [76]. The RMS average is estimated by Equation (34). Attenuation ratio, which is the relative pulsatility of the inlet pressure and outlet pressure, is also plotted for better visualization. It is computed by dividing the RMS average of the normalized outlet pressure by the RMS average of the normalized inlet pressure. The statistical analyses for all microchannel configurations accounted for 25 oscillation periods in order to maintain consistency.

$$\sigma = \sqrt{\frac{1}{n} \sum_{i=1}^n (X_i - \bar{X})^2} \quad (34)$$

The inlet conditions were assumed to be the same for the plain and the membrane microchannels because the pressure and frequency remain unchanged when testing both microchannels. Since the outlet conduits were rigid polymer tubes for all microchannels, the outlet hydraulic resistance was fixed and the pressure can be assumed to be proportional to the outlet flowrate. As a result, the measured outlet pressure is also a flowrate pulsatility indicator. Shown in Figure 19 is the measured outlet pressure wave of a plain and a membrane microchannel when subjected to a 2 Hz inlet pulsatile pressure wave. The plot shows that membrane microchannel has a lower peak-to-peak pressure

value than a plain microchannel. This indicates the membrane microchannel has lower outlet pressure pulsatility. The average outlet pressure of a membrane microchannel is slightly higher than that of a plain microchannel because the lower resistance of a membrane microchannel causes a lower pressure drop. The higher outlet pressure of a membrane microchannel suggests that a higher pressure is available along the microchannel to deform the compliant membrane microchannel wall. As indicated in Table 11, the RMS average of the outlet pressure of a membrane microchannel is lower than that of a plain microchannel. The outlet pressure plots of the 4 Hz and 6 Hz pulsatile pressure measurements are shown in Figure 20 and Figure 21 respectively. These plots also indicate lower pressure pulsatility in the membrane microchannel than in the plain microchannel. At a 6 Hz pulsatile pressure wave, the membrane microchannel has a very low RMS average outlet pressure of 31 Pa. Conversely, the plain microchannel has a RMS average outlet pressure of 62 Pa. In addition, the average outlet pressure of the membrane microchannel in these testing results is approximately 5% higher than the plain microchannel, suggesting higher pressure availability to deform the microchannel walls.

Table 11 Comparison of RMS average outlet pressure at 2 Hz, 4 Hz, 6 Hz

	Plain Microchannel	Membrane Microchannel
2 Hz	178 Pa	143 Pa
4 Hz	76 Pa	50 Pa
6 Hz	62 Pa	31 Pa

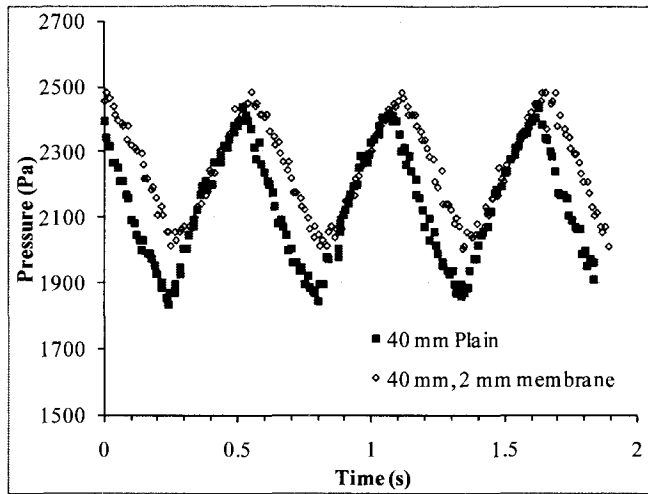


Figure 19 Outlet pressure wave of a plain vs. 2mm membrane long (40mm) microchannel at 2 Hz

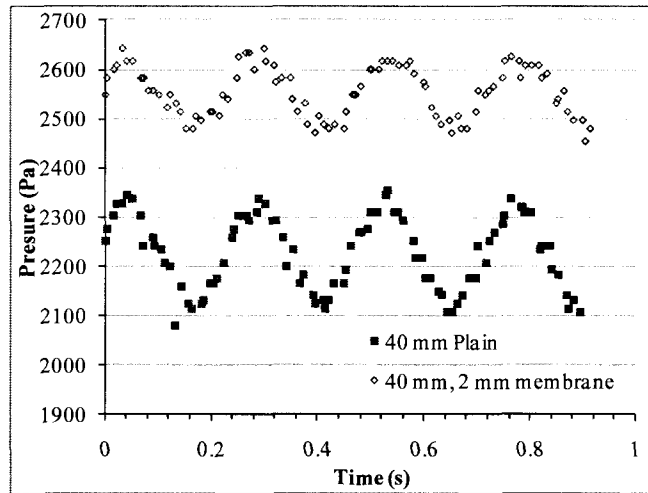


Figure 20 Outlet pressure wave of a plain vs. 2mm membrane long (40mm) microchannel at 4 Hz

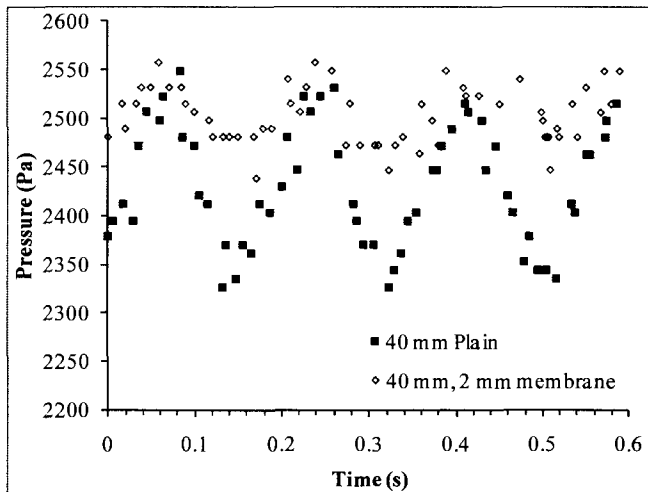
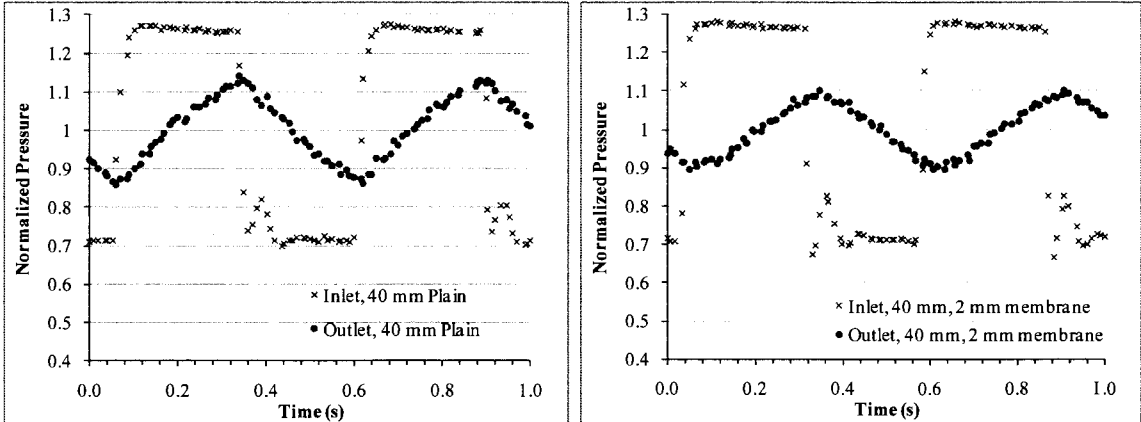


Figure 21 Outlet pressure wave of a plain vs. 2mm membrane long (40mm) microchannel at 6 Hz

The normalized inlet and outlet pressure waves of the microchannels are compared in Figure 22, Figure 23, and Figure 24. The figures on the left (a) show the response of a plain microchannel and the figures on the right (b) show the response of a membrane microchannel. Overall, for a similar inlet pressure condition, the membrane microchannels consistently show lower outlet pressure fluctuations than plain microchannels. The inlet pressure waves approximate square waves while the outlet pressure waves approximate triangle waves because of capacitance effect of a non-rigid channels. The outlet pressure lags the inlet pressure, and the phase shift is proportional to the pulsatile damping amplitude. Also, the inlet pressure rise is delayed because fluid is filling the expanded fluidic volume like a step pressure experiment.



(a) simulated plain

(b) membrane plain

Figure 22 Normalized 2 Hz inlet and outlet pressure wave.

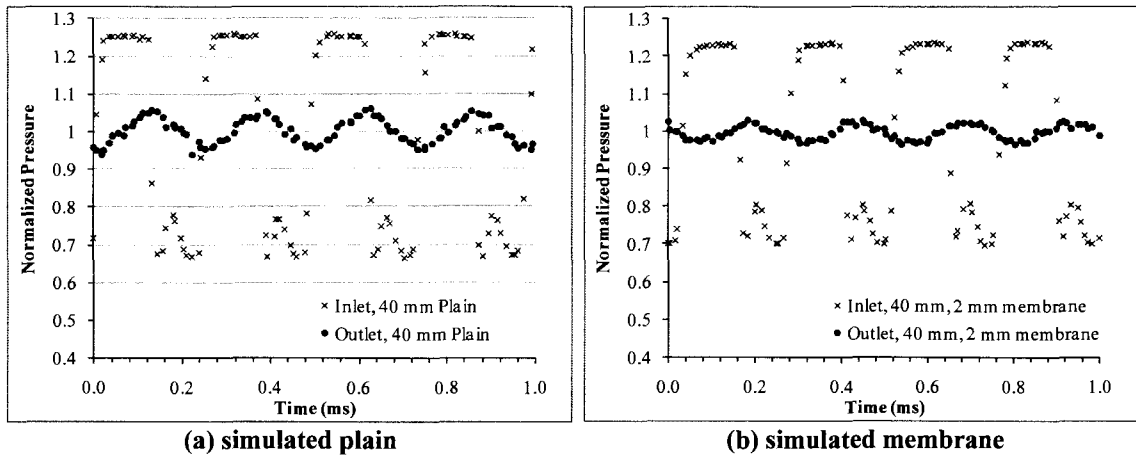


Figure 23 Normalized 4 Hz inlet and outlet pressure wave.

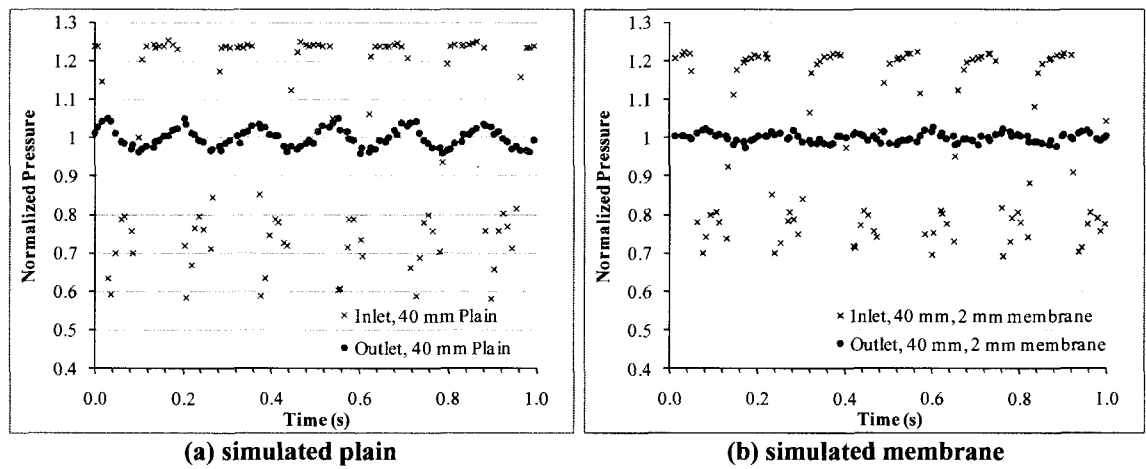


Figure 24 Normalized 6 Hz inlet and outlet pressure wave.

The pressure attenuation ratio of the normalized RMS average is also plotted in Figure 25. The pressure attenuation ratio increases with pulsatile pressure frequency on both plain and membrane microchannels. The membrane microchannel has a steeper increase in attenuation ratio compared to the plain microchannel, indicating a better pulsatile pressure damping ability throughout the high frequency. The phase-shift effects and lower outlet amplitude at high frequency confirm that the fluidic circuit is closely related to an electrical low-pass filter.

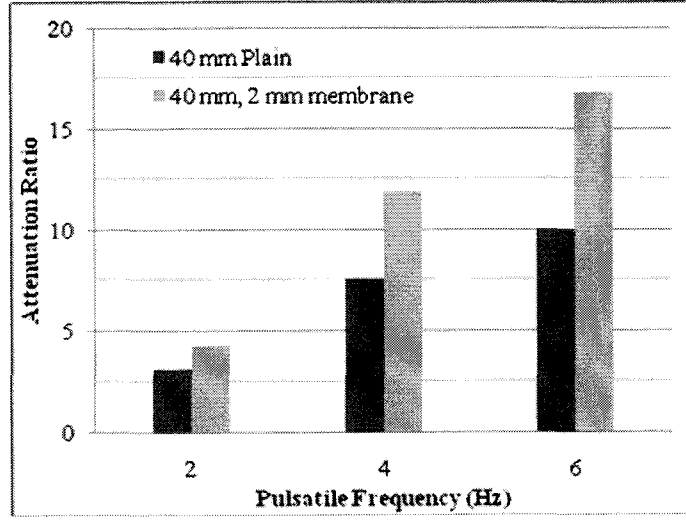


Figure 25 Attenuation ratio of the normalized RMS average of inlet and outlet pressure.

5.2 Simulation Prediction

5.2.1 Step Pressure Prediction

As described in Section 3.3.3, two levels of microchannel compliances were simulated. The 120 μm membrane geometry will be referred as the simulated membrane microchannel and the 240 μm membrane geometry will be referred as the simulated plain microchannel. The simulated step inlet pressures of the plain and membrane microchannel are plotted in Figure 26. Similar to the experimental results, simulation predicts that the membrane microchannel has a longer rise time than the plain microchannel. The normalized inlet flowrate and inlet pressure of a simulated membrane microchannel are also plotted in Figure 27. The plot shows that the inlet flowrate behaved like an under-damped system with the flowrate overshooting the set point before settling to the steady state flowrate. Comparing the changes in the inlet pressure and flowrate in response to a step pressure input, the inlet flowrate rise leads the inlet pressure rise because fluid accumulates at the expanded microchannel volume which is then followed by the rise in pressure. This behavior is analogous to the charging of an electrical capacitor, wherein the electric charge will first accumulate at the parallel plates before the voltage builds up.

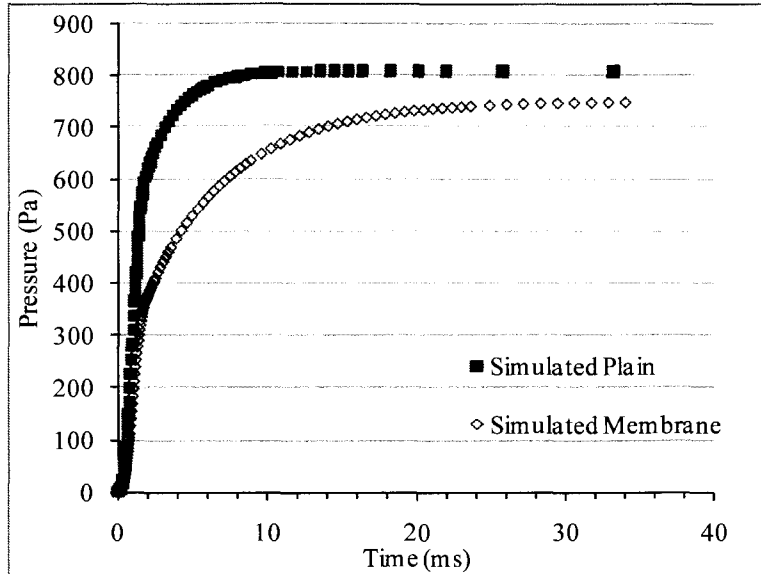


Figure 26 Inlet pressure of a simulated plain and simulated membrane microchannel due to a step pressure input.

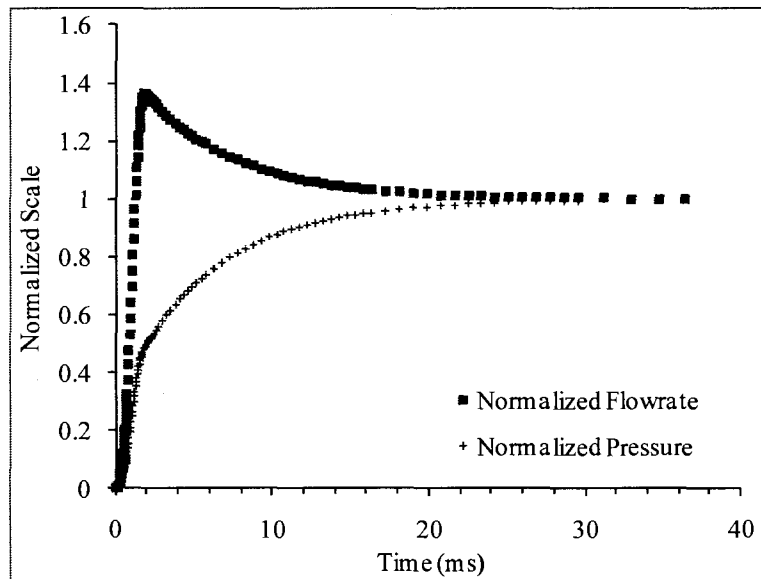
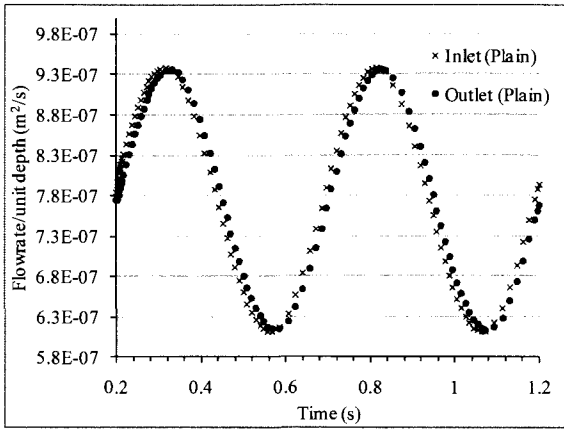


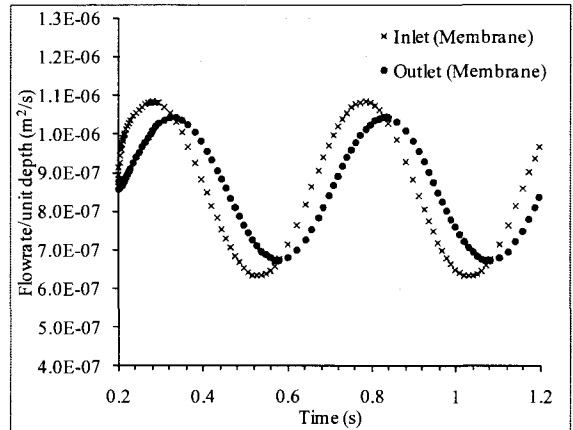
Figure 27 Plot of the normalized inlet flowrate and inlet pressure of a simulated membrane microchannel. The pressure lags the flowrate in the step pressure simulation of the compliant microchannel.

5.2.2 Pulsatile Pressure Prediction

The predicted flow stabilizations of the simulated membrane and plain microchannels are plotted in Figure 28, Figure 29 and Figure 30. The simulation predicts that the membrane microchannel has a better flow stabilization performance than the plain microchannel. This is evidenced by the ability of the membrane microchannel to reduce the peak-to-peak value of the inlet flowrate fluctuation to a lower value at the outlet than a plain microchannel. The simulated plain microchannel has a minimal peak-to-peak reduction because the rigid wall structure exhibits minimal deformation, and therefore provides very small fluidic storage. As discussed in the theory and modeling section, a rigid wall structure causes instantaneous wave propagation. Therefore, the fluctuation in the inlet flowrate is transferred to the outlet flowrate. The membrane microchannel, which has a more compliant wall structure, causes a flowrate phase shift between the inlet and outlet flowrate as evidenced in the plots. Similar to the experiment results, the simulation also predicts that the flow stabilization ratio increases with higher inlet pulsatile pressure frequencies as indicated in Figure 31. For example, at the 6 Hz pulsatile pressure case, the flowrate attenuation ratio of a simulated membrane is 2.25 while the simulated membrane attenuation ratio is 1.2. Although limited to a two-dimensional analysis, the simulation prediction is consistent with the experimental results.

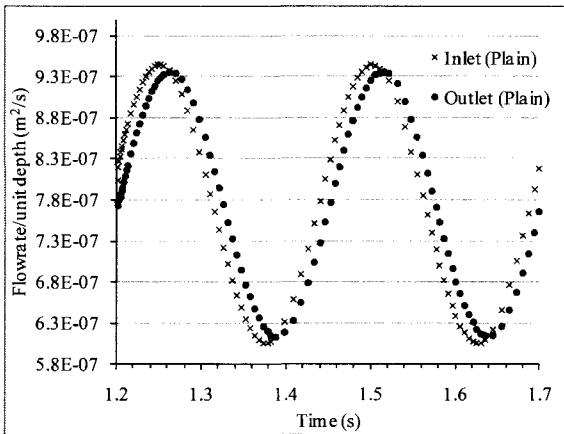


(a) Simulated plain

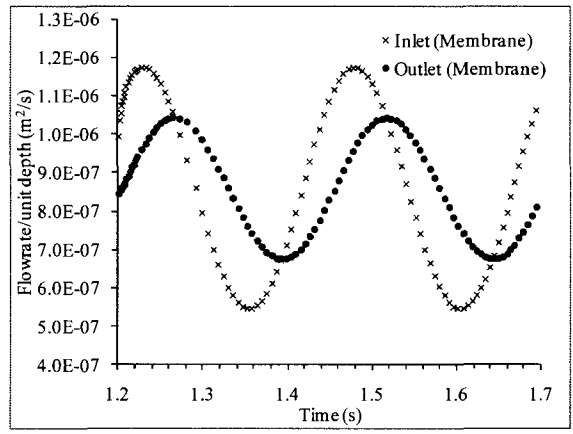


(b) Simulated membrane

Figure 28 Predicted flowrate of compliant microchannels at 2 Hz pressure wave

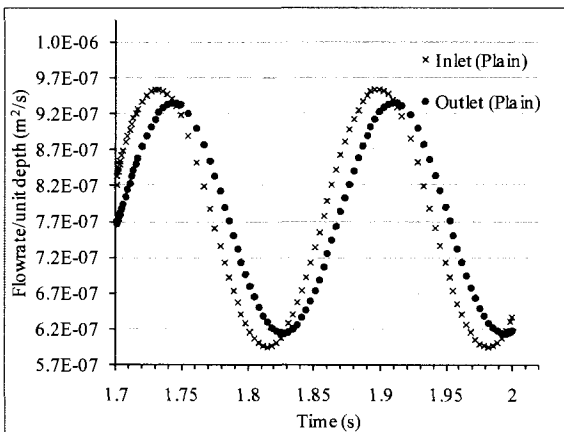


(a) Simulated plain

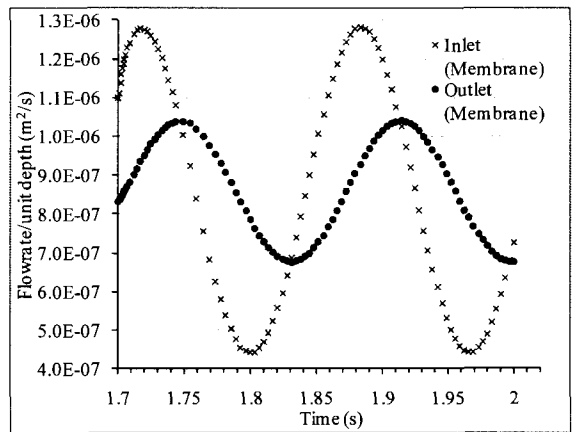


(b) Simulated membrane

Figure 29 Predicted flowrate of compliant microchannels at 4 Hz pressure wave



(a) Simulated plain



(b) Simulated membrane

Figure 30 Predicted flowrate of compliant microchannels at 6 Hz pressure wave

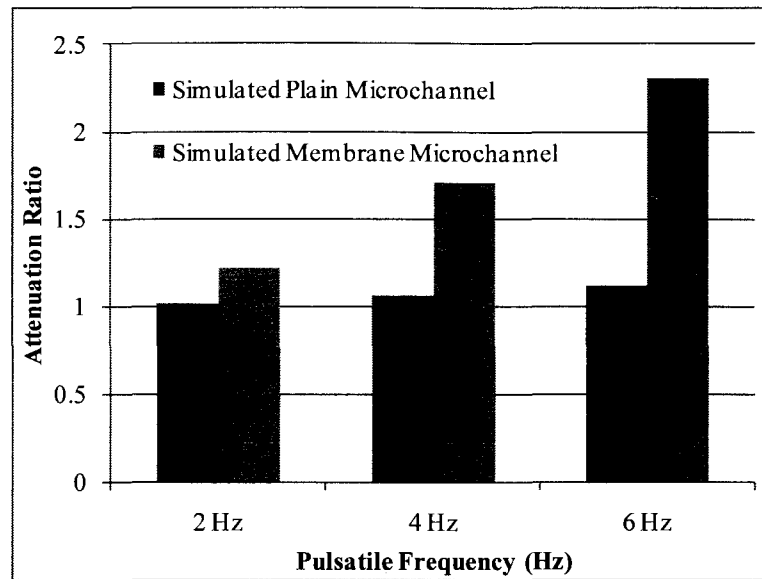


Figure 31 Flow attenuation ratio of simulated plain microchannel (left) and simulated membrane microchannel (right)

The pressure drops along a simulated plain microchannel and a simulated membrane microchannel are shown in Figure 33. The pressure drop plot is analogous to the concept of an energy grade line or a hydraulic grade line for pipe flow, which tracks the energy availability along the microchannel. The simulated membrane microchannel has a higher availability of pressure along the channel length than a plain microchannel because the expansion of the channel cross-section results in lower viscous losses. In the case of a membrane microchannel, a higher pressure is available towards the outlet and it applies more forces on the microchannel wall, causing greater overall microchannel volume expansion. Figure 32 shows a greater microchannel wall expansion in the simulated membrane microchannel than the plain microchannel. The greater wall expansion in a membrane microchannel causes a greater volume of the main flow to be diverted into the expanding microchannel cross-section.

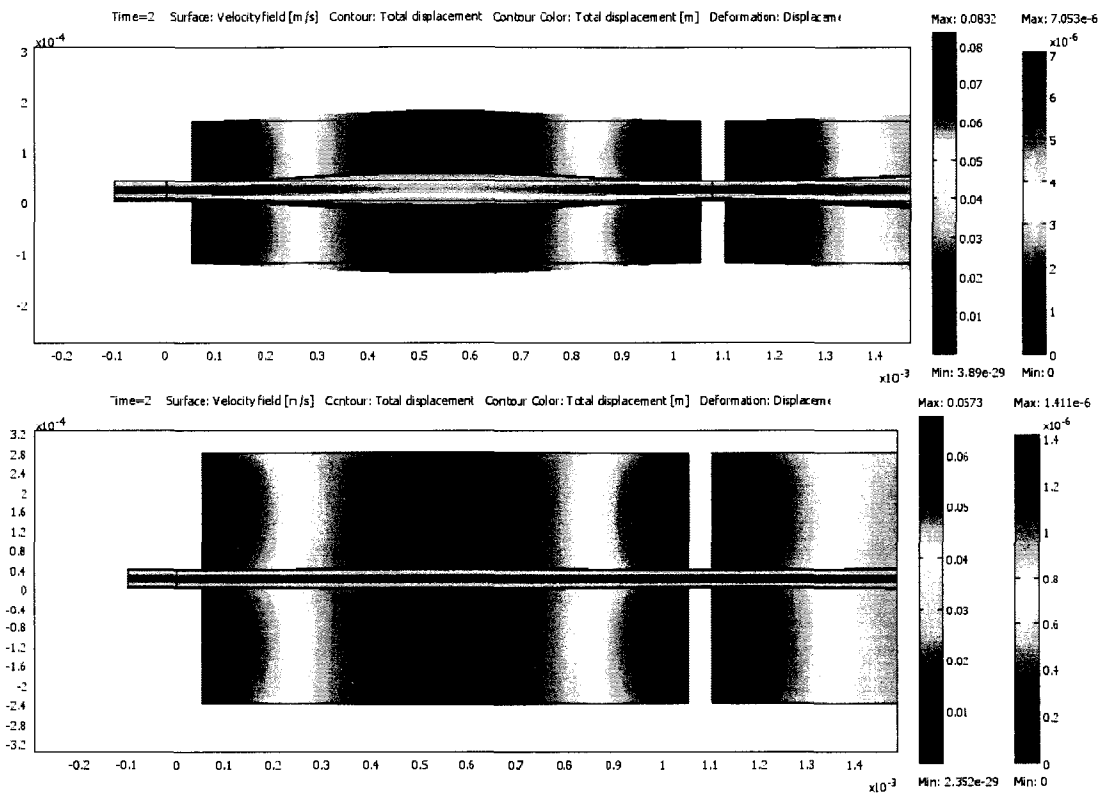


Figure 32 Simulated membrane (top), the more compliant geometry has larger deformation than simulated plain (bottom), the less compliant geometry

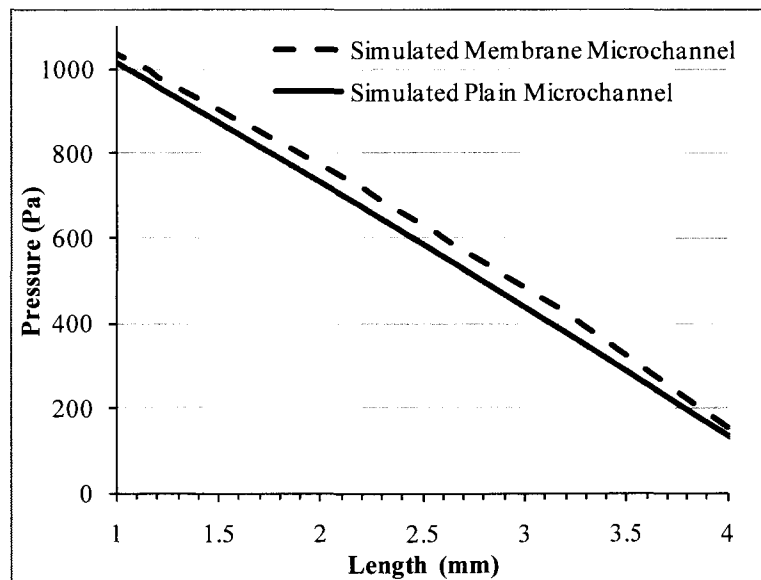


Figure 33 Pressure drop along the length of microchannel, simulated membrane microchannel vs. simulated plain microchannel

However, the overall predicted microchannel flow stabilization is lower than observed in actual experiments because of the limited ability of simulating a 3-D, full scale 40 mm microchannel. A FSI model requires finer mesh when compared to a basic structural-mechanics model to correctly account for the increases in the fluidic volume and the flow acceleration. The structural simulation is also complicated with consideration of a non-linear hyperelastic material. Solving a time-dependent FSI 3-D model would have required computing resources beyond what was available at the time of this writing. However, these results can serve as a tool to confirm measurement trends and to predict other variables that cannot be measured effectively in experiments, such as flowrate.

5.2.3 Simulation of the Cross-Section Deformation of Compliant Microchannels

A 2-D simulation study was done to examine the deformation of a microchannel wall and ceiling during a pressure driven flow. A 14 μm thick membranes microchannel cross-section and a plain microchannel cross-section were examined. The study was conducted using the plane strain application mode. A fixed boundary condition was applied to the bottom edge of the microchannel cross-section model, which simulates a permanent bond between the microfluidic chip and the glass slide. Note that the plain strain simulation assumes an infinitely long cross-section which assumes a uniform out-of-plane deformation. A parametric pressure load was applied to the surrounding channel walls. The problem was solved over a range of 0 Pa to 40 kPa with a step size of 50 kPa, using a parametric solver.

The line plot in Figure 34 shows the deformed wall profile where the horizontal axis is the perimeter of the microchannel wall and vertical axis is the displacement of the deformation. As expected, the membrane microchannel experiences a greater overall cross-sectional deformation when compared to the plain microchannel. For a 40 kPa pressure, the greatest deformation in a membrane microchannel is 1.54 μm , which is located at the side wall. Conversely, the greatest deformation in a plain microchannel is 0.85 μm , which is located at the ceiling. The observation of maximum deformation occurring at the ceiling of the plain microchannel is consistent with the findings of several research groups which studied pressure driven flow in a microchannel [39, 40]. With higher compliant channel walls, the membrane microchannel ceiling actually deforms approximately 50% more than the plain microchannel ceiling. The combined

membrane and ceiling deformation of a membrane micchannel increase the total deformed cross-sectional area over 100% compared to a plain microchannel, as evident in Table 12. To estimate the hydraulic capacitance of the compliant-wall microchannel, the deformed 2-D cross-section can be extrapolated into a 3-D deformation, by extruding the 2-D cross-section. The 2-D hydraulic capacitance is essentially the slope of the fitted line of the 2-D expanded area vs. pressure. Assuming the pressure drop along the length of the microchannel is linear, the deformed cross-sectional area decreases linearly along the length of the microchannel. With this assumption, the microchannel capacitance is calculated by multiplying the 2-D capacitance by one half the channel length. The capacitance extrapolated from simulation is $7.40 \times 10^{-17} \text{ m}^3/\text{Pa}$ for a membrane microchannel and $2.55 \times 10^{-17} \text{ m}^3/\text{Pa}$ for a plain microchannel. The capacitances extrapolated from the 2-D simulations are compared to the experimental capacitances in Table 13.

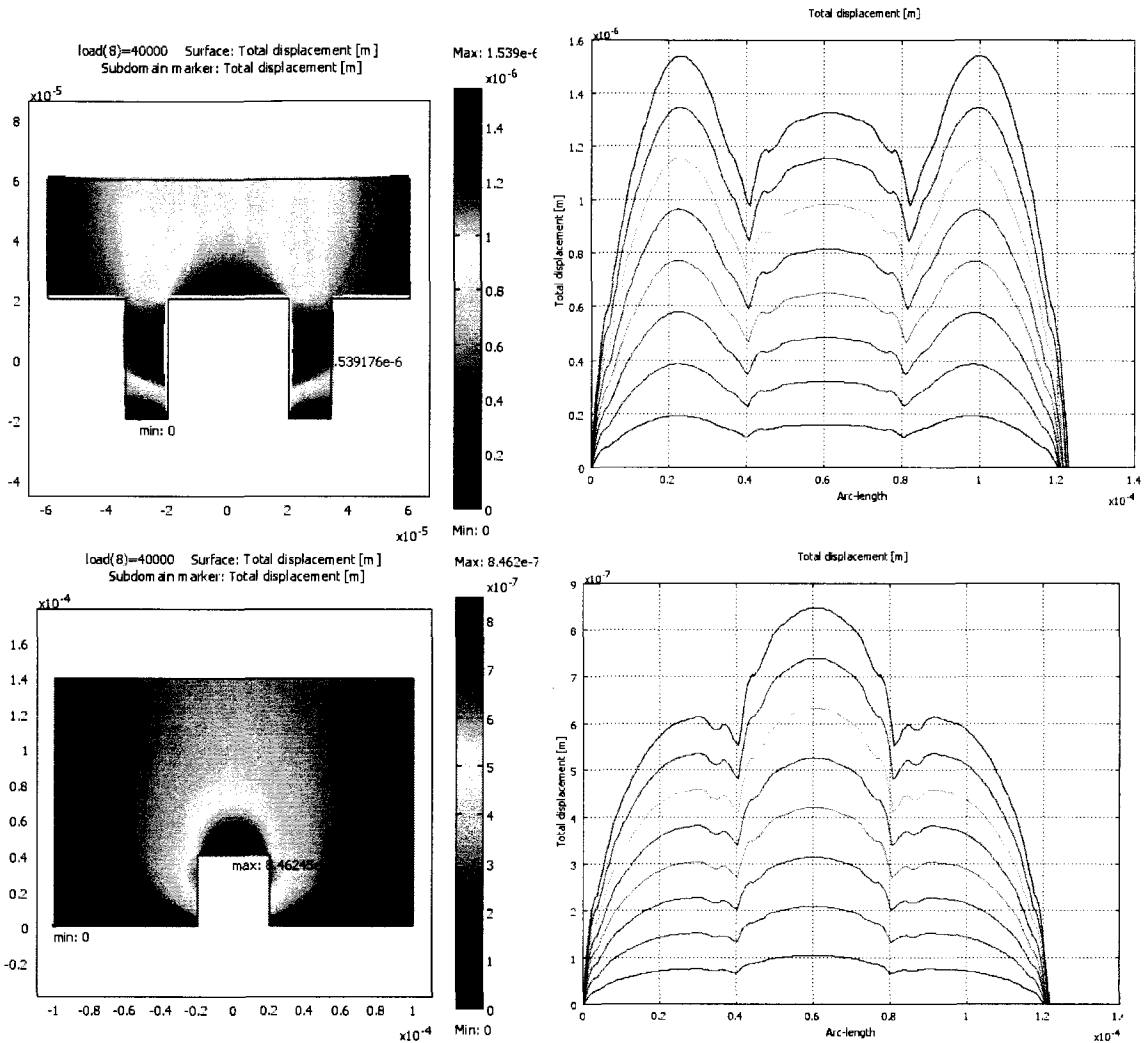


Figure 34 Simulation plots of cross-section of membrane microchannel and plain microchannel under 20 kPa load with a step size of 5000Pa. Channel cross-section is 40 μm by 40 μm .

Table 12 Comparison of expanded area of membrane channel and plain channel

Load (Pa)	Membrane Channel Area (m^2)	Plain Channel Area (m^2)
10000	3.55E-11	1.25E-11
20000	7.17E-11	2.51E-11
30000	1.09E-10	3.79E-11
40000	1.47E-10	5.09E-11

Table 13 Comparison of capacitance estimated from experimental method, and numerical method.

	Experimental Method	Numerical Method
Plain	$1.37 \times 10^{-16} \text{ m}^3/\text{Pa}$	$2.55 \times 10^{-17} \text{ m}^3/\text{Pa}$
Membrane	$2.19 \times 10^{-16} \text{ m}^3/\text{Pa}$	$7.40 \times 10^{-17} \text{ m}^3/\text{Pa}$

Comparatively, the hydraulic capacitance estimated from the simulation results is lower than the capacitance calculated from the experimental rise time measurements. The discrepancy between the experimental method and numerical method results might be attributed to several reasons. Fluid flow in a compliant microchannel is known to produce a non-linear pressure profile as discussed in Section 2.1, while the capacitance is extrapolate with the assumption of a linear pressure drop. A 3-D FSI model might better predict the hydraulic capacitance because of the greater fidelity between the simulation model and the actual device. The 3-D model might be able to reveal the non-linear pressure drop along the deformed microchannel wall and its corresponding deformation. While the target width of the fabricated membrane microchannel is 14 μm , optical profiler measurements show that the membrane cross-section has a geometry which tapered from a 14 μm width at channel ceiling to a 13 μm width at the base of membrane. The tapered sections of the membranes have unknown effects on the hydraulic resistances and capacitances values of a microchannel. Furthermore, actual PDMS material properties of the testing samples might vary from the Mooney-Rivlin hyperelastic material model. This is because PDMS is sensitive to fabrication parameters like the PDMS mixing ratio and curing conditions.

Chapter 6 Conclusion and Future Work

The use of compliant-wall microchannels for pulsatile flow attenuation had been studied. Microchannel compliance provides a hydraulic capacitance effect to the fluidic system. Hydraulic capacitance is able to dynamically increase the total fluidic volume of the microchannel. Therefore, the inlet flowrate and outlet flowrate are distinct because a portion of the inlet flowrate enters the expanded fluidic volume. The expansion of a compliant microchannel during pulsatile flow assists in the regulation of flowrate and reduces outlet pressure fluctuation.

Two levels of microchannel compliance are studied by comparing a regular plain microchannel (low compliance) and a microchannel with multiple thin-walled membranes in series (high compliance). Experiments are conducted to characterize the compliance and the pulsatile flow attenuation abilities of each microchannel. A step pressure input of 43 kPa is applied at the inlet of the microchannels. Through this experiment, the membrane microchannel is found to have a higher hydraulic capacitance which is indicated by a 40% longer rise time than that of a plain microchannel. The cutoff frequency is estimated from the rise time. The membrane microchannel and the plain microchannel are estimated to have cutoff frequencies of 1.76 Hz and 2.52 Hz respectively. A comparison metric was provided in terms of the pressure attenuation ratio which is the RMS average of the outlet pressure divided by the RMS average of the inlet pressure. The results of pulsatile pressure testing conducted over the range of 2 Hz to 6 Hz pulsatile pressure testing results revealed that the membrane microchannel has a better pulsatile pressure attenuation ratio. In a 6 Hz pulsatile pressure test, the membrane

microchannel has a higher pressure attenuation ratio of 16 while the plain microchannel has a pressure attenuation ratio of 10. The attenuation ratio of the compliant microchannel also increases with increases in the pulsatile pressure frequency. In addition, the compliant microchannel has a steeper increase in attenuation ratio at higher frequencies.

A 2-D FSI model is used to predict the flow attenuation capabilities of membrane and plain microchannels from their respective responses to a step pressure input and a pulsatile pressure input. The simulation prediction trend is in agreement with experimental results. The step pressure simulation predicts a longer rise time in the simulated membrane microchannel. Similarly, the pulsatile pressure simulation predicts better flow stabilization performance with higher channel wall compliance in a microchannel. The stabilization ratio is also predicted to increase with increases in pressure frequency. When plotting the pressure drop along the microchannel, the membrane microchannel has a lower overall pressure drop, indicating higher pressure availability along the length of the microchannel. The greater pressure availability is able to provide greater channel wall expansion by deforming more sections of the microchannel.

The simulation prediction and the experimental observation support the hypothesis that highly compliant membrane microchannels experience even greater deformation for a similar inlet pressure, hence further enhancing pulsatile flow stabilization. Traditional fluidic circuit theory models a microchannel with a fixed hydraulic resistance. This model cannot predict dynamic changes in microchannel cross-

section in response to a transient inlet pressure. In other words, it cannot account for the lower hydraulic resistance and the correspondingly higher local pressure of a microchannel. These effects are very important in designing a pulsatile flow attenuation device. Notably, the cutoff frequency is a function of hydraulic resistance and hydraulic capacitance. Note that the decrease in hydraulic resistance of a membrane microchannel is compensated with higher increase in hydraulic capacitance. From the step pressure experiment, the membrane microchannel is estimated to have approximately 10% less hydraulic resistance than a plain microchannel, but is compensated by an approximately 60% increase in hydraulic capacitance.

The findings of this study can be summarized in the following statements

- A membrane microchannel improves hydraulic capacitance by increasing structural compliance. At the same time, the increased structural compliance also decreases hydraulic resistance.
- Lower hydraulic resistance results in higher overall microchannel pressure which subsequently deforms more sections of the microchannel. This enables the higher increase of total fluidic volume to temporarily store fluid.
- The performance of a pulsatile flow attenuation device is dependent on hydraulic resistance and hydraulic capacitance. A membrane microchannel has higher increase in hydraulic capacitance than hydraulic resistance.

Some of the areas for future work that would build upon the work of this thesis are optimizing microchannel compliance and refining the compliant-conduit flow model. From the results, it is clear that fluidic stabilization improves with higher compliance,

thus it is desirable to engineer the membrane to have higher compliance. A direct method of increasing compliance is by fabricating thinner and taller membranes. This has been shown to have significantly increase membrane deformation under pressure loading [38]. These structural requirements translate into high-aspect ratio SU-8 photolithography. High-aspect ratio photolithography, however, requires more stringent fabrication processes. For example, a chrome-glass photomask is known to have excellent photolithographic resolution but costs significantly more than a mylar film based photomask. Photolithographic process parameters including UV light exposure dosage, bake time, and development time would require optimization to identify the best settings for improving resolution. There are also alternative methods of increasing compliance. The microchannels can be designed to be wider to exploit ceiling deformation as a source of fluidic capacitance. A ceiling expansion cavity can also be integrated along the microchannel with a single layer soft-photolithography step or by stacking a very thin PDMS sheet on top of the microchannel cavities [50]. The PDMS thickness which determines the compliance of the conduit can be controlled by spin-coating PDMS onto the SU-8 mold or by dispensing a smaller amount of PDMS during the casting process. Since PDMS has a tunable modulus of elasticity, it can be mixed with a higher ratio of PDMS pre-polymer base to curing agent. This will produce a softer PDMS polymer which enhances the compliance of the microchannel. However, any passive flow stabilizer that is based on deformable structures requires higher pressure to function optimally. This effect can be circumvented by having an advanced pressure feedback system that actively changes the pressures acting on the other side of the membranes.

Vacuum or pneumatic systems can be used for flow stabilization by introducing an opposing pressure wave through actuation of the membranes which would have the effects of countering incoming pulsatile waves. The pulsatile flow damping system can also be optimized so that the natural frequency of the membrane is similar to the pulsatile pressure frequency. The natural frequency of the microchannel can be found through a structural FEA frequency analysis. At the natural frequency, the membrane would have significantly higher deflection, thus reducing the number of membranes required to achieve a required fluidic capacitance. These mentioned alternative designs can be pursued in the future.

Since conventional hydraulic circuit modeling theory often assumes a fixed hydraulic resistance, it will yield inaccurate results and would require consideration of a variable hydraulic resistance. A FSI numerical model would be able to predict the variable hydraulic resistance and hydraulic capacitance of the compliant conduit. However, a full scale 3-D FSI model is very difficult to solve when given a full-length microchannel and the requirement of a fine mesh throughout the model. Faster and higher efficient computing in the future is expected to mitigate this limitation, which will allow for a full-field solution. Presently, a 2-D simulation is able to provide a limited prediction of the pulsatile flow stabilization capabilities of a compliant microchannel. In addition, a lumped parameter model with a variable resistance correction factor might be an intermediate solution.

Bibliography

- [1] D. Erickson and D. Li, "Integrated microfluidic devices," *Analytica Chimica Acta*, vol. 507, pp. 11-26, 2004.
- [2] T. Thorsen, S. J. Maerkl, and S. R. Quake, "Microfluidic Large-Scale Integration," *Science*, vol. 298, pp. 580-584, October 18, 2002 2002.
- [3] P. Abgrall and A. M. Gue, "Lab-on-chip technologies: making a microfluidic network and coupling it into a complete microsystem-a review," *Journal of Micromechanics and Microengineering*, vol. 17, pp. R15-R49, 2007.
- [4] P. S. Dittrich, K. Tachikawa, and A. Manz, "Micro Total Analysis Systems. Latest Advancements and Trends," *Analytical Chemistry*, vol. 78, pp. 3887-3908, 2006.
- [5] Y. Wang, W.-Y. Lin, K. Liu, R. J. Lin, M. Selke, H. C. Kolb, N. Zhang, X.-Z. Zhao, M. E. Phelps, C. K. F. Shen, K. F. Faull, and H.-R. Tseng, "An integrated microfluidic device for large-scale in situ click chemistry screening," *Lab on a Chip*, vol. 9, pp. 2281-2285, 2009.
- [6] S. H. DeWitt, "Micro reactors for chemical synthesis," *Current Opinion in Chemical Biology*, vol. 3, pp. 350-356, 1999.
- [7] K.-T. J. Yeo, A. H. B. Wu, F. S. Apple, M. H. Kroll, R. H. Christenson, K. B. Lewandrowski, F. A. Sedor, and A. W. Butch, "Multicenter evaluation of the Roche NT-proBNP assay and comparison to the Biosite Triage BNP assay," *Clinica Chimica Acta*, vol. 338, pp. 107-115, 2003.

- [8] H. Dongeun, G. Wei, K. Yoko, B. G. James, and T. Shuichi, "Microfluidics for flow cytometric analysis of cells and particles," *Physiological Measurement*, p. R73, 2005.
- [9] P. S. Dittrich and A. Manz, "Lab-on-a-chip: microfluidics in drug discovery," *Nat Rev Drug Discov*, vol. 5, pp. 210-218, 2006.
- [10] S. Kaushik, A. H. Hord, D. D. Denson, D. V. McAllister, S. Smitra, M. G. Allen, and M. R. Prausnitz, "Lack of Pain Associated with Microfabricated Microneedles," *Anesth Analg*, vol. 92, pp. 502-504, February 1, 2001 2001.
- [11] B. Ziaie, A. Baldi, M. Lei, Y. Gu, and R. A. Siegel, "Hard and soft micromachining for BioMEMS: review of techniques and examples of applications in microfluidics and drug delivery," *Advanced Drug Delivery Reviews*, vol. 56, pp. 145-172, 2004.
- [12] D. A. LaVan, D. M. Lynn, and R. Langer, "TIMELINE: Moving smaller in drug discovery and delivery," *Nature Reviews Drug Discovery*, vol. 1, p. 77, 2002.
- [13] T. M. Squires and S. R. Quake, "Microfluidics: Fluid physics at the nanoliter scale," *Reviews of Modern Physics*, vol. 77, pp. 977-50, 2005.
- [14] J. P. Brody and P. Yager, "Diffusion-based extraction in a microfabricated device," *Sensors and Actuators A: Physical*, vol. 58, pp. 13-18, 1997.
- [15] J. Stasiak, S. Richards, and S. Angelos, "Hewlett Packard's inkjet MEMS technology: past, present, and future," in *Micro- and Nanotechnology Sensors, Systems, and Applications*, Orlando, FL, USA, 2009, pp. 73180U-5.

- [16] S. Yao, D. E. Hertzog, S. Zeng, J. C. Mikkelsen, and J. G. Santiago, "Porous glass electroosmotic pumps: design and experiments," *Journal of Colloid and Interface Science*, vol. 268, pp. 143-153, 2003.
- [17] J. Linan, J. Mikkelsen, K. Jae-Mo, D. Huber, Y. Shuhuai, Z. Lian, Z. Peng, J. G. Maveety, R. Prasher, J. G. Santiago, T. W. Kenny, and K. E. Goodson, "Closed-loop electroosmotic microchannel cooling system for VLSI circuits," *Components and Packaging Technologies, IEEE Transactions on*, vol. 25, pp. 347-355, 2002.
- [18] E. Kjeang, N. Djilali, and D. Sinton, "Microfluidic fuel cells: A review," *Journal of Power Sources*, vol. 186, pp. 353-369, 2009.
- [19] H.-F. Li and J.-M. Lin, "Applications of microfluidic systems in environmental analysis," *Analytical and Bioanalytical Chemistry*, vol. 393, pp. 555-567, 2009.
- [20] A. A. Alexeenko, D. A. Fedosov, S. F. Gimeishein, D. A. Levin, and R. J. Collins, "Transient Heat Transfer and Gas Flow in a MEMS-Based Thruster," *Journal of Microelectromechanical Systems*, vol. 15, pp. 181-194, 2006.
- [21] H. Becker and L. E. Locascio, "Polymer microfluidic devices," *Talanta*, vol. 56, pp. 267-287, 2002.
- [22] N.-T. Nguyen and S. T. Wereley, *Fundamentals and applications of microfluidics*. Boston, MA: Artech House, 2002.
- [23] D. C. Duffy, J. C. McDonald, O. J. A. Schueller, and G. M. Whitesides, "Rapid Prototyping of Microfluidic Systems in Poly(dimethylsiloxane)," *Anal. Chem.*, vol. 70, pp. 4974-4984, 1998.

- [24] G. M. Whitesides, "The origins and the future of microfluidics," *Nature*, vol. 442, pp. 368-373, 2006.
- [25] A. Mata, A. Fleischman, and S. Roy, "Characterization of Polydimethylsiloxane (PDMS) Properties for Biomedical Micro/Nanosystems," *Biomedical Microdevices*, vol. 7, pp. 281-293, 2005.
- [26] N. Sundararajan, D. Kim, and A. A. Berlin, "Microfluidic operations using deformable polymer membranes fabricated by single layer soft lithography," *Lab on a Chip*, vol. 5, pp. 350-354, 2005.
- [27] B. Yang, G. C. Lopez, Q. Lin, and A. J. Rosenbloom, "Microfabricated PDMS Check Valves," *ASME International Mechanical Engineering Congress* vol. 5, pp. 369-372, 2003.
- [28] C. H. Ahn, C. Jin-Woo, G. Beaucage, J. H. A. N. J. H. Nevin, A. J.-B. L. Jeong-Bong Lee, A. A. P. A. Puntambekar, and J. Y. A. L. J. Y. Lee, "Disposable smart lab on a chip for point-of-care clinical diagnostics," *Proceedings of the IEEE*, vol. 92, pp. 154-173, 2004.
- [29] D. J. Laser and J. G. Santiago, "A review of micropumps," *Journal of Micromechanics and Microengineering*, p. R35, 2004.
- [30] S.-Y. Yang, S.-K. Hsiung, Y.-C. Hung, C.-M. Chang, T.-L. Liao, and G.-B. Lee, "A cell counting/sorting system incorporated with a microfabricated flow cytometer chip," *Measurement Science and Technology*, vol. 17, pp. 2001-2009, 2006.

- [31] N.-T. Nguyen, X. Huang, and T. K. Chuan, "MEMS-Micropumps: A Review," *Journal of Fluids Engineering*, vol. 124, pp. 384-392, 2002.
- [32] T. A. Neff, J. E. Fischer, G. Schulz, O. Baenziger, and M. Weiss, "Infusion pump performance with vertical displacement: effect of syringe pump and assembly type," *Intensive Care Medicine*, vol. 27, pp. 287-291, 2001.
- [33] F. Lin, W. Saadi, S. W. Rhee, S. J. Wang, S. Mittal, and N. L. Jeon, "Generation of dynamic temporal and spatial concentration gradients using microfluidic devices," *Lab Chip*, vol. 4, 2004.
- [34] A. A. Desmukh, D. Liepmann, and A. P. Pisano, "Continuous micromixer with pulsatile micropumps," Hilton Head Island, SC, USA, 2000, pp. 73-6.
- [35] D. Ateya, J. Erickson, P. Howell, L. Hilliard, J. Golden, and F. Ligler, "The good, the bad, and the tiny: a review of microflow cytometry," *Analytical and Bioanalytical Chemistry*, vol. 391, pp. 1485-1498, 2008.
- [36] J. S. Eugen Cabuz, Bob DeMers, Ernie Satren, Aravind Padmanabhan, & Cleo Cabuz, "MEMS-Based Flow Controller for Flow Cytometry," in *Solid-State Sensor, Actuator and Microsystems Workshop*, Hilton Head Island, SC, 2002, pp. 110-111.
- [37] W. J. Lough and I. W. Wainer, *High performance liquid chromatography : fundamental principles and practice*. London; New York: Blackie Academic & Professional, 1996.
- [38] S. J. Lee, J. C. Y. Chan, K. J. Maung, E. Rezler, and N. Sundararajan, "Characterization of laterally deformable elastomer membranes for

- microfluidics," *Journal of Micromechanics and Microengineering*, vol. 17, pp. 843-851, 2007.
- [39] T. Gervais, J. El-Ali, A. Gunther, and K. F. Jensen, "Flow-induced deformation of shallow microfluidic channels," *Lab on a Chip*, vol. 6, pp. 500-507, 2006.
- [40] B. Hardy, K. Uechi, J. Zhen, and P. Kavehpour, "The deformation of flexible PDMS microchannels under a pressure driven flow," *Lab Chip*, vol. 9, pp. 935-938, 2009.
- [41] M. Akbari, D. Sinton, and M. Bahrami, "Pressure Drop in Rectangular Microchannels as Compared With Theory Based on Arbitrary Cross Section," *Journal of Fluids Engineering*, vol. 131, pp. 041202-8, 2009.
- [42] M. A. Holden, S. Kumar, A. Beskok, and P. S. Cremer, "Microfluidic diffusion diluter: bulging of PDMS microchannels under pressure-driven flow*," *Journal of Micromechanics and Microengineering*, p. 412, 2003.
- [43] S. Wu, J. Mai, Y. Zohar, Y. C. Tai, and C. M. Ho, "A suspended microchannel with integrated temperature sensors for high-pressure flow studies," in *Micro Electro Mechanical Systems, 1998. MEMS 98. Proceedings., The Eleventh Annual International Workshop on*, 1998, pp. 87-92.
- [44] G. Oates, "Fluid flow in soft-walled tubes part 1: Steady flow," *Medical and Biological Engineering and Computing*, vol. 13, pp. 773-779, 1975.
- [45] S. R. Reuben, "Compliance of the Human Pulmonary Arterial System in Disease," *Circulation Research*, vol. 29, pp. 40-50, 1971.
- [46] V. c. Tesar, *Pressure-driven Microfluidics*. Boston: Artech House, 2007.

- [47] D. Kim, N. Chesler, and D. Beebe, "A method for dynamic system characterization using hydraulic series resistance," *Lab Chip*, vol. 6, pp. 639-644, 2006.
- [48] W. Inman, K. Domansky, J. Serdy, B. Owens, D. Trumper, and L. G. Griffith, "Design, modeling and fabrication of a constant flow pneumatic micropump," *Journal of Micromechanics and Microengineering*, vol. 17, pp. 891-899, 2007.
- [49] Y. Bozhi, J. L. Metier, and L. Qiao, "Using compliant membranes for dynamic flow stabilization in microfluidic systems," in *Micro Electro Mechanical Systems, 2005. MEMS 2005. 18th IEEE International Conference on*, 2005, pp. 706-709.
- [50] Y. Bozhi and L. Qiao, "A Compliance-Based Microflow Stabilizer," *Microelectromechanical Systems, Journal of*, vol. 18, pp. 539-546, 2009.
- [51] B. Yang and Q. Lin, "Planar micro-check valves exploiting large polymer compliance," *Sensors and Actuators A: Physical*, vol. 134, pp. 186-193, 2007.
- [52] B. Yang and Q. Lin, "A Planar Compliance-Based Self-Adaptive MicrofluidVariable Resistor," *Microelectromechanical Systems, Journal of*, vol. 16, pp. 411-419, 2007.
- [53] P. Cousseau, R. Hirschi, B. Frehner, S. Gamper, and D. Maillefer, "Improved micro-flow regulator for drug delivery systems," in *Micro Electro Mechanical Systems, 2001. MEMS 2001. The 14th IEEE International Conference on*, 2001, pp. 527-530.
- [54] J. Atencia and D. J. Beebe, "Steady flow generation in microcirculatory systems," *Lab Chip*, vol. 6, 2006.

- [55] V. Namasivayam, R. G. Larson, D. T. Burke, and M. A. Burns, "Transpiration-based micropump for delivering continuous ultra-low flow rates," *Journal of Micromechanics and Microengineering*, vol. 13, pp. 261-271, 2003.
- [56] S. Takayama, E. Ostuni, P. LeDuc, K. Naruse, D. E. Ingber, and G. M. Whitesides, "Laminar flows: Subcellular positioning of small molecules," *Nature*, vol. 411, pp. 1016-1016, 2001.
- [57] T. T. Perkins, D. E. Smith, R. G. Larson, and S. Chu, "Stretching of a Single Tethered Polymer in a Uniform Flow," *Science*, vol. 268, pp. 83-87, 1995.
- [58] B. Yang and Q. Lin, "Three-dimensional FEM simulation of a microfluidic diode considering coupled fluid-structure interaction," Chicago, IL, United States, 2006, p. 4.
- [59] A. Klein, S. Matsumoto, and G. Gerlach, "Modeling and design optimization of a novel micropump," in *International Conference on Modeling and Simulation of Microsystems, Semiconductors, Sensors and Actuators*, Santa Clara, CA, USA, 1998, pp. 506 - 511.
- [60] O. C. Jeong and S. Konishi, "The self-generated peristaltic motion of cascaded pneumatic actuators for micro pumps," *Journal of Micromechanics and Microengineering*, vol. 18, p. 085017, 2008.
- [61] J. G. Korvink and O. Paul, *MEMS: a practical guide to design, analysis, and applications*. New York: Springer, 2006.

- [62] L. Qiao, Y. Bozhi, X. Jun, and T. Yu-Chong, "Dynamic simulation of a peristaltic micropump considering coupled fluid flow and structural motion," *Journal of Micromechanics and Microengineering*, p. 220, 2007.
- [63] J. Xie, J. Shih, Q. Lin, B. Yang, and Y. C. Tai, "Surface micromachined electrostatically actuated micro peristaltic pump," *Lab Chip*, vol. 4, 2004.
- [64] C. Berli, "Equivalent circuit modeling of electrokinetically driven analytical microsystems," *Microfluidics and Nanofluidics*, vol. 4, pp. 391-399, 2008.
- [65] H. Bruus, *Theoretical Microfluidics*. Oxford: Oxford University Press, 2008.
- [66] R. M. Kirby, G. E. Karniadakis, O. Mikulchenko, and K. Mayaram, "An integrated simulator for coupled domain problems in MEMS," *Microelectromechanical Systems, Journal of*, vol. 10, pp. 379-391, 2001.
- [67] R. J. Adrian, "Particle-Imaging Techniques for Experimental Fluid Mechanics," *Annual Review of Fluid Mechanics*, vol. 23, pp. 261-304, 1991.
- [68] J. G. Santiago, S. T. Wereley, C. D. Meinhart, D. J. Beebe, and R. J. Adrian, "A particle image velocimetry system for microfluidics," *Experiments in Fluids*, vol. 25, pp. 316-319, 1998.
- [69] C. D. Meinhart, S. T. Wereley, and M. H. B. Gray, "Volume illumination for two-dimensional particle image velocimetry," *Measurement Science and Technology*, vol. 11, pp. 809-814, 2000.
- [70] F. M. White, *Fluid mechanics*. Boston [u.a.]: McGraw-Hill Higher Education, 2008.

- [71] T. C. Papanastasiou, G. C. Georgiou, and A. N. Alexandrou, *Viscous fluid flow*. Boca Raton, FL: CRC Press, 2000.
- [72] M. Zamir, *The Physics of Coronary Blood Flow*: Springer, 2005.
- [73] J. R. Womersley, "Method for the calculation of velocity, rate of flow and viscous drag in arteries when the pressure gradient is known," *The Journal of Physiology*, vol. 127, pp. 553-563, 1955.
- [74] M. Zamir, *The Physics of Pulsatile Flow*: Springer, 2000.
- [75] G. Oates, "Fluid flow in soft-walled tubes Part 2: Behaviour of finite waves," *Medical and Biological Engineering and Computing*, vol. 13, pp. 780-784, 1975.
- [76] P. M. Meenen and R. Adhami, *Fundamental concepts in electrical and computer engineering*. Boca Raton, FL: Universal Pub., 2005.
- [77] R. J. Roark, W. C. Young, and R. G. Budynas, *Roark's formulas for stress and strain*. New York: McGraw-Hill, 2002.
- [78] C. Morris and F. Forster, "Oscillatory flow in microchannels," *Experiments in Fluids*, vol. 36, pp. 928-937, 2004.
- [79] T. Hu and J. P. Desai, "Characterization of Soft-Tissue Material Properties: Large Deformation Analysis," in *Medical Simulation*, 2004, pp. 28-37.
- [80] P. J. Prendergast, C. Lally, S. Daly, A. J. Reid, T. C. Lee, D. Quinn, and F. Dolan, "Analysis of Prolapse in Cardiovascular Stents: A Constitutive Equation for Vascular Tissue and Finite-Element Modelling," *Journal of Biomechanical Engineering*, vol. 125, pp. 692-699, 2003.

- [81] R. Medicine Meets Virtual and J. D. Westwood, "Medicine meets virtual reality 14 : accelerating change in healthcare : next medical toolkit," Amsterdam; Washington, DC.
- [82] M. J. G. Ruíz and L. Y. S. González, "Comparison of hyperelastic material models in the analysis of fabrics," *International Journal of Clothing Science and Technology*, vol. 18, pp. 314-325, 2006.
- [83] M. F. Beatty, "Topics in Finite Elasticity: Hyperelasticity of Rubber, Elastomers, and Biological Tissues---With Examples," *Applied Mechanics Reviews*, vol. 40, pp. 1699-1734, 1987.
- [84] Y.-S. Yu and Y.-P. Zhao, "Deformation of PDMS membrane and microcantilever by a water droplet: Comparison between Mooney-Rivlin and linear elastic constitutive models," *Journal of Colloid and Interface Science*, vol. 332, pp. 467-476, 2009.
- [85] R. S. Rivlin, G. I. Barenblatt, and D. D. Joseph, *Collected papers of R.S. Rivlin*. New York: Springer, 1997.
- [86] R. European Conference on Constitutive Models for, A. Dorfmann, and A. H. Muhr, "Constitutive models for rubber : proceedings of the First European Conference on Constitutive Models for Rubber, Vienna, Austria, 9-10 September 1999," Rotterdam, Netherlands; Brookfield, VT, USA.
- [87] Comsol, *COMSOL Multiphysics Version 3.4 Reference Guide*. Burlington, Mass.: COMSOL, 2007.

- [88] G. T. Mase and G. E. Mase, *Continuum mechanics for engineers*. Boca Raton, Fla.: CRC Press, 1999.
- [89] I. Ansys, *ANSYS® Release 11.0, Help System, Chapter 8. Nonlinear Structural Analysis*. [Canonsburg, PA]: ANSYS, 2007.
- [90] A. C. Robinson, T. A. Brunner, S. Carroll, R. Drake, C. J. Garasi, T. Gardiner, T. Hail, H. Hanshaw, D. Hensinger, and D. Labreche, "ALEGRA: An Arbitrary Lagrangian-Eulerian Multimaterial, Multiphysics Code."
- [91] E. Stein, R. d. Borst, and T. J. R. Hughes, "Encyclopedia of computational mechanics," Chichester, West Sussex: John Wiley, 2004.
- [92] O. C. Zienkiewicz, R. L. Taylor, P. Nithiarasu, and J. Z. Zhu, *The finite element method*. Oxford; New York: Elsevier/Butterworth-Heinemann, 2005.
- [93] M. Martinelli and V. Viktorov, "Modelling of laminar flow in the inlet section of rectangular microchannels," *Journal of Micromechanics and Microengineering*, vol. 19, p. 025013, 2009.
- [94] M. Gad-el-Hak, "The MEMS handbook," in *The Mechanical engineering handbook series* Boca Raton, FL: CRC Press, 2002.
- [95] P. Moin, *Fundamentals of engineering numerical analysis*. Cambridge, UK; New York: Cambridge University Press, 2001.
- [96] D. C. Duffy, O. J. A. Schueller, S. T. Brittain, and G. M. Whitesides, "Rapid prototyping of microfluidic switches in poly(dimethyl siloxane) and their actuation by electro-osmotic flow," *Journal of Micromechanics and Microengineering*, vol. 9, pp. 211-217, 1999.

- [97] MicroChem, "Processing Guidelines For:SU-8 2025, SU-8 2035, SU-8 2050 and SU-8 2075," Ver.4 Retrieved Feb/26/2009.
- [98] A. J. Wheeler and A. R. Ganji, *Introduction to Engineering Experimentation*, 2nd ed. Upper Saddle River, N.J.: Prentice Hall, Inc., 2004.
- [99] K. Ogata, *Modern control engineering*. Upper Saddle River, NJ: Prentice Hall, 2002.
- [100] S. Keller, G. Blagoi, M. Lillemose, D. Haefliger, and A. Boisen, "Processing of thin SU-8 films," *Journal of Micromechanics and Microengineering*, vol. 18, p. 125020, 2008.
- [101] T. A. Anhoj, A. M. Jorgensen, D. A. Zauner, J. bner, and rg, "The effect of soft bake temperature on the polymerization of SU-8 photoresist," *Journal of Micromechanics and Microengineering*, vol. 16, pp. 1819-1824, 2006.

Appendix I Optimization of SU-8 Fabrication

Early stages of SU-8 photolithography fabrication yielded poor and unusable SU-8 molds. Notably, the narrow region of SU-8 had poor clearance (Figure 35) and the SU-8 structure was not adhering to substrate. Several fabrication parameters such as age of SU-8 photoresists, age of SU-8 developer, intensity of UV lamp, quality of UV filter, quality of photomask, SU-8 baking time and temperature were identified as potential cause of the problems. The troubleshooting effort focused on the baking process, since the baking time was unusually long when compared to Microchem's recommended procedures [97].

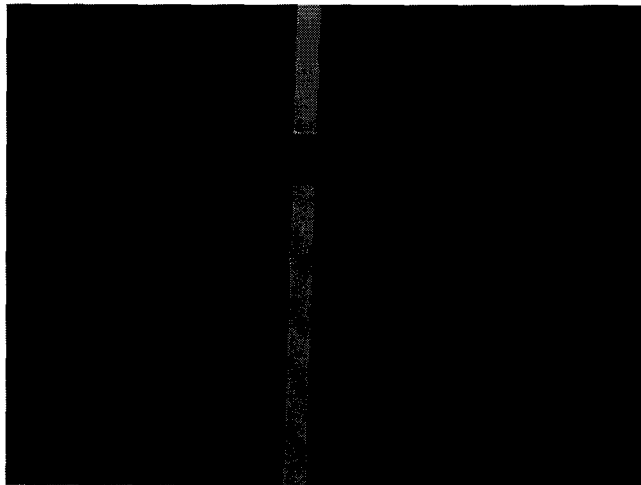


Figure 35 Picture shows section of SU-8 structure with poor photolithography resolution. The 10 μm gap for thin microchannel walls did not clear properly. The surface of the SU-8 structure had severe cracking.

Note that the poor SU-8 fabrication results were done using the SU-8 2050 processing procedure developed earlier at the SJSU MEMSLAB. The current SU-8 used is SU-8 2035, which has higher solvent content and lower viscosity, as shown in Table 14. Thus, it was initially thought that the softbaking time to evaporate the solvent would

be somewhat longer compared to SU-8 2050 using a similar processing procedure. However, previous baking steps were done on an aluminum-foil warped hot plate to avoid stubborn SU-8 residue. The foil usually traps a thin layer of air between the hot plate and foil, causing uncertainty in true contact temperature and inconsistent temperature distribution. Hence, the soft-bake and post-bake time were extended and required constant monitoring of SU-8 “stickiness”.

Table 14 Viscosity comparison between SU-8 2035 and 2050 [97]

SU-8 2000	% Solids	Viscosity (cSt)
2035	69.95	7000
2050	71.65	12900

Although soft baking reduces the amount of solvent in the spin-coated SU-8, a sufficient amount of solvent or photo-acid generator triarylsulfonium hexafluoroantimonate needs to be retained [100, 101]. When the photo-acid generator is exposed to UV light, it decomposes and hydrogen ions are generated to initiate cross-linking. Post-baking of the SU-8 structure further accelerates and promotes photo-acid diffusion and monomer mobility, enhancing cross-linking [100]. Excellent temperature and time control is required to trap acid species in the exposed area and prevent future diffusion into unexposed areas to improve resolution. This is also known as the cage effect [100].

A bare flat aluminum plate with temperature feedback was also introduced in recent fabrication process to enhance temperature uniformity when baking. With an aluminum plate with temperature feedback, the temperature was closer to true set

temperature. The combined effects of an increase in SU-8 solvent content and introduction of an aluminum contact plate caused the optimum processing windows to shift. Shorter soft-bake and post-bake time was found to yield excellent SU-8 adhesion to the silicon wafer. The baking time is summarized in Table 15.

Table 15 Comparison of original and optimized baking time

	Original Baking Time	Optimized Baking Time
Soft-Bake (65°C)	3 min	3 min
Soft-Bake (95°C)	60 min, ramped from 65°C	5 min
Post-Bake (65°C)	4 min	1 min
Post-Bake (95°C)	10 min, ramped from 65°C	5 min

Appendix II SU-8 Fabrication Log

PPM Microfluidic Chips Updated 2009 Jan 15 Thur 10:20
MicroChem SU-8 2035, LOT 08050401, exp date: 6/1/2009
MicroChem SU-8 Developer, LOT 07080541, exp date: 8/1/2009

Bare Silicon <100>, Diameter 100 mm, thickness 600-650 μm
P-type (Boron), resistivity 10-20 $\text{ohm}\cdot\text{cm}$
From Montco Silicon Technologies, Inc., Lot #5216, 2006 May 12
Piranha cleaned 12/19

Wafer 1: 090115-01 Exposure Calibration Mask
Wafer 2: 090115-02 Mask 12 μm 09011412
Wafer 3: 090115-03 Mask 14 μm 09011414
Wafer 4: 090115-04 Mask 14 μm 09011414

SU-8 Wafer Fabrication Process Steps

1020 UV lamp turned on
 Calculate target doses provided in Table 1
1034 Singe wafer #01, 02 on hotplate at 150 °C for 5 min
1039 Removed wafer #01 and 02 from hotplate and place in wafer case
1041 Singe wafer #03, 04 on hotplate at 150 °C for 5 min
1046 Removed wafer #03 and 04 from hotplate and place in wafer case
1058 Clean Spin wafer #01 500 rpm for 15 s plus 2500 rpm for 40 s
1059 Pour SU-8 on wafer #01, Spin Coat wafer #01 500 rpm for 15 s plus 2500 rpm for 40 s
1100 Place Wafer #01 on hot plate at 65°C for 3 min
1103 Place Wafer #01 on hot plate at 95°C for 5 min
1108 Remove wafer #01 from hotplate and let cool for 9 min
1117 Expose wafer #01 according to values in Table 1
1127 Place Wafer #01 on hot plate at 65°C for 1 min
1128 Place Wafer #01 on hot plate at 95°C for 5 min
1133 Remove wafer #01 from hotplate and let cool for 16 min
1149 Develop wafer #01 for 7 mins
1136 Clean Spin wafer #02 500 rpm for 15 s plus 2500 rpm for 40 s
1137 Pour SU-8 on wafer #02, Spin Coat wafer #01 500 rpm for 15 s plus 2500 rpm for 40 s
1138 Place Wafer #02 on hot plate at 65°C for 3 min
1141 Place Wafer #02 on hot plate at 95°C for 5 min
1146 Remove wafer #02 from hotplate and let cool for 44 min

1139 Clean Spin wafer #03 500 rpm for 15 s plus 2500 rpm for 40 s
1140 Pour SU-8 on wafer #03, Spin Coat wafer #01 500 rpm for 15 s plus 2500 rpm for 40 s
1141 Place Wafer #03 on hot plate at 65°C for 3 min
1144 Place Wafer #03 on hot plate at 95°C for 5 min
1150 Remove wafer #03 from hotplate and let cool for min
1145 Clean Spin wafer #04 500 rpm for 15 s plus 2500 rpm for 40 s
1146 Pour SU-8 on wafer #04, Spin Coat wafer #01 500 rpm for 15 s plus 2500 rpm for 40 s
1147 Place Wafer #04 on hot plate at 65°C for 3 min
1152 Place Wafer #04 on hot plate at 95°C for 5 min
1157 Remove wafer #04 from hotplate and let cool for min
1230 Expose wafer #02 with mask at 5.20 mW/cm² for 34.6 s (180 mJ/cm²)
1231 Place Wafer #02 on hot plate at 65°C for 1 min
1232 Place Wafer #02 on hot plate at 95°C for 5 min
1237 Remove wafer #02 from hotplate and let cool for 37 min
1314 Develop wafer #02 for 7 mins
1335 Expose wafer #04 at 5.20 mW/cm² for 34.6 s (180 mJ/cm²)
1337 Place Wafer #04 on hot plate at 65°C for 1 min
1338 Place Wafer #04 on hot plate at 95°C for 5 min
1343 Remove wafer #04 from hotplate and let cool for 10 min
1405 Develop wafer #04 for 7 mins
1425 Expose wafer #03 at 5.20 mW/cm² for 34.6 s (180 mJ/cm²)
1426 Place Wafer #03 on hot plate at 65°C for 1 min
1427 Place Wafer #03 on hot plate at 95°C for 5 min
1433 Remove wafer #03 from hotplate and let cool for 10 min
1445 Develop wafer #03 for 7 mins